Aphelion water-ice cloud mapping and property retrieval using the OMEGA imaging spectrometer onboard Mars Express

Jean-Baptiste Madeleine, Francois Forget, Aymeric Spiga, Michael J. Wolff, Franck Montmessin, Mathieu Vincendon, Denis Jouglet, Brigitte Gondet, Jean-Pierre Bibring, Yves Langevin, et al.

Aphelion water-ice cloud mapping and property retrieval using the OMEGA imaging spectrometer onboard Mars Express

J.-B. Madeleine,[1,2] F. Forget,[1] A. Spiga,[1] M. J. Wolff,[3] F. Montmessin,[4] M. Vincendon,[5] D. Jouglet,[5] B. Gondet,[5] J.-P. Bibring,[5] Y. Langevin,[5] and B. Schmitt[6]

Received 19 August 2011; revised 13 February 2012; accepted 5 March 2012; published 9 May 2012.

[1] Mapping of the aphelion clouds over the Tharsis plateau and retrieval of their particle size and visible opacity are made possible by the OMEGA imaging spectrometer aboard Mars Express. Observations cover the period from MY26 $L_s = 330°$ to MY29 $L_s = 180°$ and are acquired at various local times, ranging from 8 AM to 6 PM. Cloud maps of the Tharsis region constructed using the 3.1 μm ice absorption band reveal the seasonal and diurnal evolution of aphelion clouds. Four distinct types of clouds are identified: *morning hazes*, *topographically controlled hazes*, *cumulus clouds* and *thick hazes*. The location and time of occurrence of these clouds are analyzed and their respective formation process is discussed. An inverse method for retrieving cloud particle size and opacity is then developed and can only be applied to *thick hazes*. The relative error of these measurements is less than 30% for cloud particle size and 20% for opacity. Two groups of particles can be distinguished. The first group is found over flat plains and is composed of relatively small particles, ranging in size from 2 to 3.5 μm. The second group is characterized by particle sizes of $\sim$5 μm which appear to be quite constant over L_s and local time. It is found west of Ascraeus and Pavonis Mons, and near Lunae Planum. These regions are preferentially exposed to anabatic winds, which may control the formation of these particles and explain their distinct properties. The water ice column is equal to 2.9 pr.μm on average, and can reach 5.2 pr.μm in the thickest clouds of Tharsis.

Citation: Madeleine, J.-B., et al. (2012), Aphelion water-ice cloud mapping and property retrieval using the OMEGA imaging spectrometer onboard Mars Express, *J. Geophys. Res.*, *117*, E00J07, doi:10.1029/2011JE003940.

1. Introduction

> *"I have often noticed occasional changes of partial bright belts* (…) *and also once a darkish one, in a pretty high latitude* (…). *And these alterations we can hardly ascribe to any other cause than the variable disposition of clouds and vapours floating in the atmosphere of that planet."*
>
> [*Herschel*, 1784, p. 273]

[2] More than two centuries after the pioneering observations of William Herschel, the flotilla of satellites orbiting the red planet provides an unique opportunity to discover their detailed properties and better understand their formation process.

[3] Characterizing the morphology and microphysical properties of Martian clouds is key to understand many processes at various scales. First, clouds play a major role in the water cycle by modulating the flux of water vapor from one hemisphere to the other [*Clancy et al.*, 1996; *Richardson et al.*, 2002]. Therefore, a good knowledge of their properties is necessary to accurately predict the water cycle in global climate models [*Montmessin et al.*, 2004]. Second, cloud properties are sensitive meteorological indicators. They reflect the dynamical, temperature, humidity and aerosol conditions of the air parcel in which they formed. Then, clouds absorb and scatter the solar and infrared radiation, thereby impacting on the atmospheric temperature and dynamics [*Haberle et al.*, 1999; *Colaprete and Toon*, 2000; *Hinson and Wilson*, 2004; *Wilson et al.*, 2008]. They also play a key role in the atmospheric chemistry, by heterogeneous reactions with gaseous species [*Lefèvre et al.*, 2008]. Finally, the cloud properties reflect their detailed microphysics, and give an opportunity to investigate the processes of nucleation and crystal growth in a different environment than the Earth [*Michelangeli et al.*, 1993; *Colaprete et al.*, 1999; *Määttänen et al.*, 2005; *Iraci et al.*, 2010].

[4] Changes in cloud properties occur both on seasonal and diurnal bases. The diurnal changes are amplified by the large diurnal temperature variations of Mars, and cloud

[1]Laboratoire de Météorologie Dynamique, CNRS/UPMC/IPSL, Paris, France.
[2]Now at the Department of Geological Sciences, Brown University, Providence, Rhode Island, USA.
[3]Space Science Institute, Boulder, Colorado, USA.
[4]LATMOS, CNRS/UVSQ/IPSL, Guyancourt, France.
[5]Institut d'Astrophysique Spatiale, Orsay, France.
[6]Laboratoire de Planétologie de Grenoble, UJF/CNRS, Grenoble, France.

0148-0227/12/2011JE003940

properties can be expected to vary drastically over the course of a day. This is particularly true for aphelion clouds which are the focus of this paper. Their seasonal variations are now well-known, but the same cannot be said for diurnal variations. Apart from the early analyses by *Curran et al.* [1973] (revisited by *Zasova et al.* [2001]) and *Petrova et al.* [1996], the most complete study of cloud properties to date was made by *Clancy et al.* [2003] and *Wolff and Clancy* [2003], who used the Thermal Emission Spectrometer of Mars Global Surveyor (TES/MGS) to constrain the particle size and opacity of clouds for hundreds of Emission Phase Functions (EPFs). This data set has good spatial and seasonal coverage, but is limited in local time, since the sun-synchronous orbit of MGS only permits retrievals at 2 PM (2 AM observations are difficult to handle in the thermal infrared because of the reduced surface-atmosphere thermal contrast). *Tamppari et al.* [2003] focused on the diurnal evolution of cloud coverage using the Viking Infrared Thermal Mapper (IRTM), but did not have the possibility to retrieve cloud particle size and opacity. Another attempt has been made by *Glenar et al.* [2003], who looked at the Martian clouds at Kitt Peak Observatory over three nights, allowing to follow the evolution of aphelion clouds over 6 Martian hours at $L_s = 130°$. Unfortunately, this method was not able to distinguish particle sizes greater than 4 μm.

[5] The OMEGA (Observatoire pour la Minéralogie, l'Eau, les Glaces et l'Activité) imaging spectrometer of Mars Express gives the opportunity to bridge these gaps. First, the Mars Express orbit allows retrieval of cloud properties at various local times, ranging from 8 AM to 6 PM. Secondly, the spectral range includes the 1.5, 2, and 3.1 μm absorption bands of water ice, giving sufficient spectral information to measure cloud particle sizes greater than 4 μm.

[6] This paper is thus an attempt to refine our knowledge of the diurnal evolution of aphelion clouds. To do so, regional cloud maps are constructed and a method to retrieve cloud particle size and opacity is developed. The following questions are then addressed:

[7] 1. What is the diurnal variation in cloud cover and morphology in the Tharsis region?

[8] 2. How do the corresponding particle sizes and optical thicknesses evolve?

[9] 3. How can we interpret these observations in the light of the regional climate conditions?

[10] To answer these questions, we focus on the area of Tharsis where cloud occurrence is the largest. This corresponds to the quadrant formed by the coordinates 30°S–127°W/42°N–55°W [see, e.g., *Benson et al.*, 2003, Figure 6b]. After describing the OMEGA instrument (section 2), we first map the clouds in the Tharsis region using a simple spectral ratio and over three Martian years (MY27 to MY29). In doing so, we outline the changes in the cloud cover and morphology for different periods and local times (section 3). Then, we extend the analysis by developing a retrieval algorithm of cloud particle size and opacity. In subsequent sections, we detail the limits and uncertainties of the method (section 4.1 and Appendix A) and analyze the space and time evolution of the cloud microphysical properties (section 4.2). All the results are finally discussed in the light of our present knowledge of cloud microphysics and Martian global climate (section 5). In the concluding section, we summarize the main results and answer the above three questions.

2. The OMEGA Near-Infrared Imaging Spectrometer

2.1. Spacecraft Orbit

[11] The orbit of Mars Express was chosen to provide good observing conditions both during daytime (optical systems) and nighttime (radar sounding). The orbit pericenter moves over the planet, at an altitude of around 300 km, covering regions at various local times. The orbit is nearly polar, having an inclination of ~86.6° [*Hechler and Yanez*, 2003]. It was in 11:3 resonance (i.e. the spacecraft returns to the same latitude after 11 orbits and 3 sols, with a slight change in longitude) until the end of 2007, when it switched to a 15:8 resonance. In our study, only nadir observations are considered, and correspond to the parts of the orbit where altitude is lower than 4500 km [see *Langevin et al.*, 2007, Figure 2].

2.2. Instrument Characteristics

[12] OMEGA is an imaging spectrometer that provides spectral image cubes (x, λ, y) of the atmosphere and the surface. Wavelength ranges from 0.35 to 5.1 μm, using three different channels and a total of 352 spectels. These three channels are called "visible" (0.35–1.05 μm), "C" (1–2.77 μm) and "L" (2.65–5.1 μm).

[13] The visible channel is built in a pushbroom configuration, whereas C and L sensors operate in a whiskbroom mode. The altitude of the spacecraft ranges from 300 to 4500 km during nadir observations. Consequently, the swath width is changed to 16, 32, 64 or 128 pixels, in order of increasing altitude. The instantaneous field of view (IFOV) is equal to 1.2 mrad, resulting in a spatial resolution of ~0.35–5.4 km. The swath width thus ranges from ~5 km to ~600 km, giving access to cloud regional distribution as well as local morphological details.

[14] Spectral resolution $\lambda/2\Delta\lambda$ ranges from 50 to 100, corresponding to a $\Delta\lambda$ of ~0.013–0.02 μm. The signal over noise ratio (S/N) is at least equal to 100 over the entire spectrum [*Bibring et al.*, 2004]. Further technical details on the instrument are given in Appendix A.

2.3. Observing Period

[15] The observations used in this paper cover the period from January 2004 to the end of December 2008. Following the chronology of *Clancy et al.* [2000] (with the first Martian year beginning on April 11, 1955), this approximately corresponds to the end of MY26 ($L_s = 330°$) through the middle of MY29 ($L_s = 180°$). Consequently, three aphelion seasons are analyzed at different local times for MY27, 28, and 29.

2.4. Measured Physical Quantity

[16] From raw OMEGA data in DN (Digital Number), the OMEGA software (employing version 7) computes a radiance I_Ω (W m^{-2} μm^{-1} sr^{-1}). In reflectance spectroscopy, this radiance is then divided by the solar radiance at Mars distance to give the radiance factor r_F. Assuming a

Lambertian surface, the spherical reflectance r_s is equal to the normal albedo A_N and

$$r_s = A_N = \frac{r_F}{\mu_0} = \frac{I_\Omega}{\mu_0 I_{Sun}}, \quad (1)$$

where μ_0 is the cosine of the incidence angle. This quantity is extensively used hereinafter and referred simply as "reflectance".

3. Regional Mapping of Aphelion Clouds

[17] In this section, we introduce the so-called cloud index and describe the data set used to map the clouds in the Tharsis region. Then, we describe the seasonal and diurnal evolution of the cloud coverage in this region. The corresponding maps are given in Figures 1 and 2. These observations are summarized in section 3.5, and interpreted in section 5.1.

3.1. Spectral Ratio Used for Cloud Mapping

[18] The clouds are mapped using the visible channel of OMEGA and a spectral ratio computed at longer wavelengths, called the cloud index. The cloud index is given by the ratio of the reflectance at 3.4 μm to the reflectance at 3.52 μm, and was first introduced by *Langevin et al.* [2007]. It reflects the slope on the edge of the 3.1 μm band. When water ice is present, the slope on the edge of the 3.1 μm band increases and the cloud index therefore decreases. The color scale of Figures 1 and 2 thus ranges from white for a cloud index of 0.8 to dark blue for a cloud index of 0.4 (see the color scale in the lower right corner of Figure 3). The shades of blue give an indication of the cloud particle size and opacity. Using synthetic cloud spectra, we computed the values of the cloud index for different cloud properties. The light blue color starts to appear when the size of the ice particles is larger than $\sim$0.5 μm, and when the visible opacity of the cloud is larger than $\sim$0.1. Then, the blue color gets darker as cloud particle size and/or opacity increases. A deep blue color is reached when the visible opacity of the cloud is larger than unity, as can be seen for example in Figure 3b. Most of the aphelion clouds have a light blue color, which corresponds to a cloud index of around 0.7 and a visible optical depth of around 0.4. However, this simple spectral ratio is not sufficient to determine cloud properties in detail. Indeed, a given value of the cloud index can correspond to either a thin cloud of large particles, or a relatively thicker cloud of smaller particles. To obtain an accurate measurement of the cloud properties, it is necessary to fit the whole spectrum using the other absorption bands at 1.5 and 2 μm, as will be done in section 4.

3.2. Analyzed Data Set

[19] Only nadir observations ($e < 7°$) are selected for our study and low incidence pixels ($i > 84°$) are removed. Maps are constructed for MY27, 28 and 29 (from orbit 243 to orbit 6396), and local time always varies from one observation to the next. This is illustrated by Figure 4, which shows the local time of all OMEGA observations used to construct the cloud index maps. It shows that for a given period in L_s, the Tharsis region has been observed at a different local time each year.

[20] The interannual variability of the aphelion cloud belt appeared to be low in many previous studies [e.g., *Benson et al.*, 2003; *Smith*, 2004, section 4.2 and Figure 16; *Benson et al.*, 2006]. One exception is MY27, during which a low latitude local dust storm changed the cloud cover around $L_s = 135°$ [*Smith*, 2009]. The storm was located around 25°E though, outside the region analyzed here. We therefore assume that if two OMEGA observations are acquired at two different years at the same location and L_s, but at different local times, then the changes in cloud properties between the two observations are mainly caused by the difference in local time. Likewise, we assume that if two observations are acquired at two different years at the same location and local time, but at two different L_s, then the changes in cloud properties between the two observations stem from the difference in L_s. Keeping this in mind, Figure 4 shows many groups of orbits that can be used to monitor both seasonal and diurnal changes in cloud properties. We thus selected different pairs of observations in which these changes are seen. They are represented by boxes in Figures 1 and 2. Red boxes correspond to observations that are close in local time LT (less than one hour difference) but acquired at different L_s. Black boxes indicate regions that were covered by OMEGA at the same L_s (less than 5° difference), but at different local times.

[21] In the next two sections, we describe the observed seasonal (red boxes) and diurnal (black boxes) variations, respectively.

3.3. Seasonal Evolution

[22] From the comparison of different observations that were acquired at various L_s but at about the same local time, the main development stages of the aphelion cloud belt can be described as follows:

[23] 1. The onset of the aphelion cloud belt is clearly seen by comparing Figures 1a and 1b. Both red boxes of Figure 1a show regions that are devoid of any detectable clouds at 11 AM and $L_s \simeq 20°$. About 20° of L_s later, thin hazes appear in these regions, as shown in Figure 1b. This transition corresponds to the onset of the aphelion cloud belt, described, for example, by *Wang and Ingersoll* [2002], *Benson et al.* [2003], *Smith* [2004], *Mateshvili et al.* [2007], and *Clancy et al.* [2003, Figure 12]. A closer look at these *morning hazes* is shown in Figure 3a, where they are seen surrounding Pavonis Mons in early morning (LT = 8.5).

[24] 2. A clear evolution in cloud index is seen when comparing Figures 1d and 1e. Three regions, indicated by the red boxes, can be compared accurately, and show an increase in the cloud spatial extent and index over a 30° L_s period. Fields of cumulus clouds are present in the western part of Alba Patera and north of Pavonis Mons at 1 PM and $L_s = 53°$. These cumulus clouds are relatively thin, and are 5 to 10 km in size. It is worth noting that we use the term "cumulus" only to describe the morphology of these clouds. This term usually implies a convective origin, which is only suggested in this paper. As will be discussed in section 5, the convective origin needs to be confirmed, and the term "cumulus clouds" will be used in this paper only to refer to the cumuliform shape of the clouds. They can be compared to those observed in early summer at 3.5 PM by *Leovy et al.* [1973, Figure 14] near Ascraeus Mons (at that time called "North Spot"). An example of these cumulus clouds is given in Figure 3d. Diffuse clouds also surround Pavonis and Arsia Mons. 35° of L_s later (Figure 1e), at the same local time,

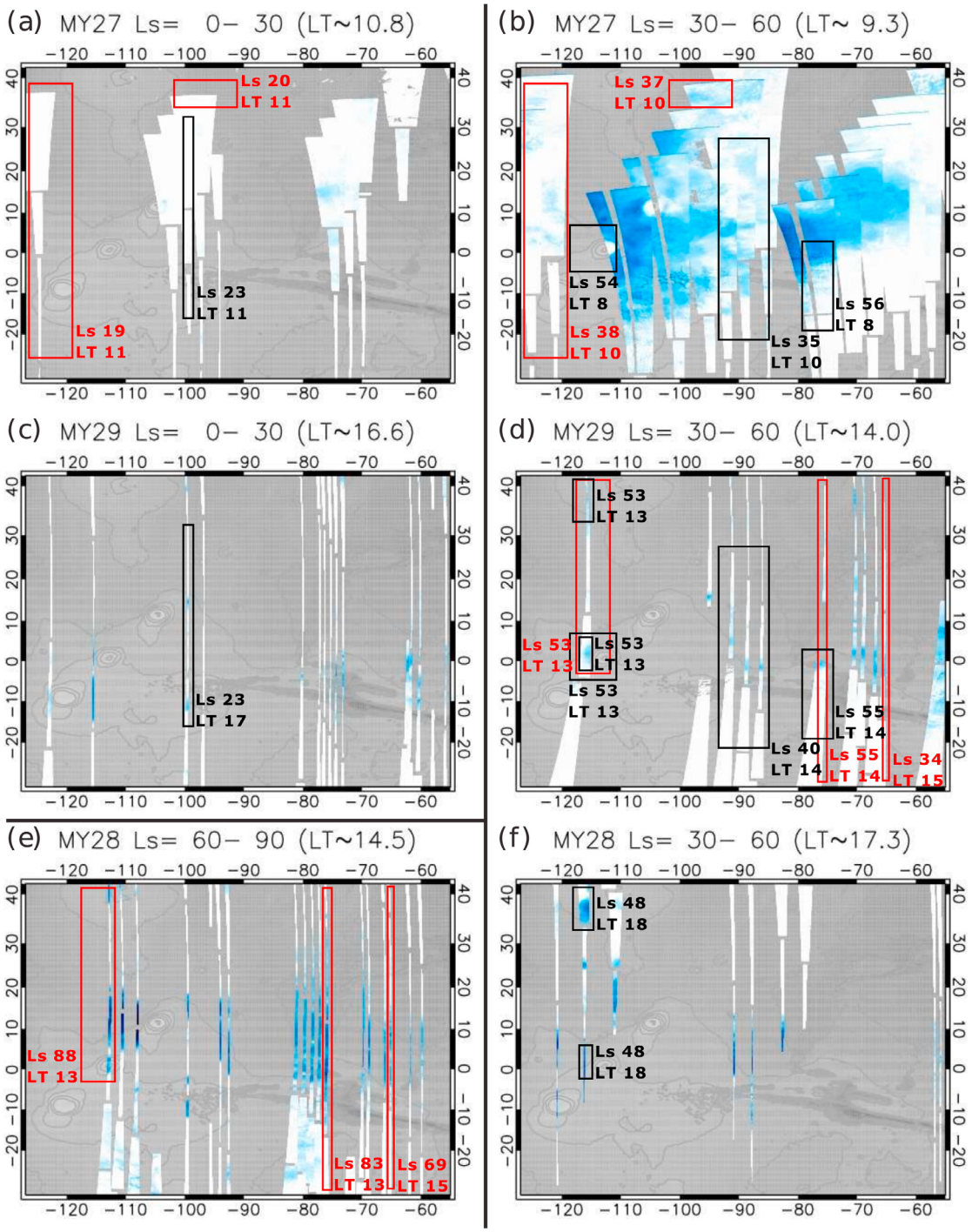

Figure 1. Cloud index maps (see section 3) for intervals of 30° of L_s. Diurnal variations can be appreciated between Figures 1a and 1c for the L_s = 0–30° period, and between Figures 1b, 1d, and 1f for the L_s = 30–60° period. Only one set of observations is available for the L_s = 60–90° period (Figure 1e). Red boxes indicate the regions that were observed at different L_s but at the same local time LT (less than one hour difference) from one year to another. On the contrary, black boxes show particular regions that were observed at different local times but at the same L_s (less than 5° difference). For all the maps presented in this paper, the background grey scale is the MOLA (Mars Orbiter Laser Altimeter) topography [*Zuber et al.*, 1992].

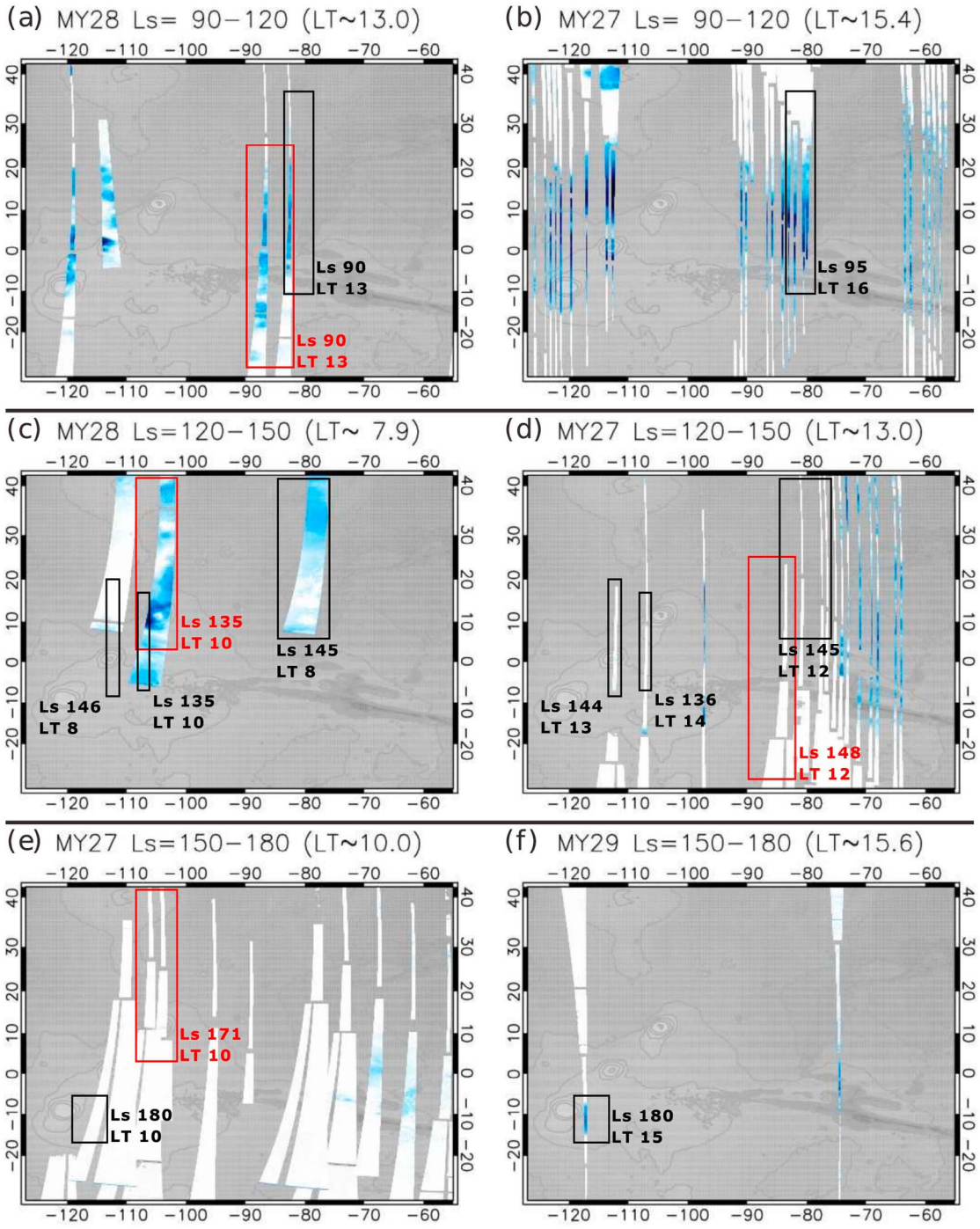

Figure 2. Same as Figure 1 for the (a and b) L_s = 90–120°, (c and d) L_s = 120–150°, and (e and f) L_s = 150–180° periods.

cumulus clouds are still present north of Pavonis Mons and near Alba Patera, but are now associated with a thick haze layer (red box on the left). The diffuse clouds of Pavonis Mons are also thicker than at L_s = 53°. The same sequence is discernable, although less obvious, in the two other regions indicated by the red boxes around 75°W and 65°W in Figures 1d and 1e.

[25] In summary, it seems that during mid-spring, the beginning of the afternoon is characterized by localized cumulus clouds that are accompanied by the formation of a thick haze layer later in the season. It is consistent with the Mariner 9 observations of *Kahn* [1984], who noted the presence in northern spring of "thin hazes", which "increase in thickness late in the season". The thickest clouds are found around L_s = 100°, as depicted in Figure 2b. It is consistent with the analysis of *Benson et al.* [2003], who found a peak in the cloud area at the same L_s.

[26] 3. The decay of the aphelion cloud belt is visible in Figures 2a–2d and 2c–2e. Early summer (Figure 2a) is characterized by cumulus clouds that are similar to those

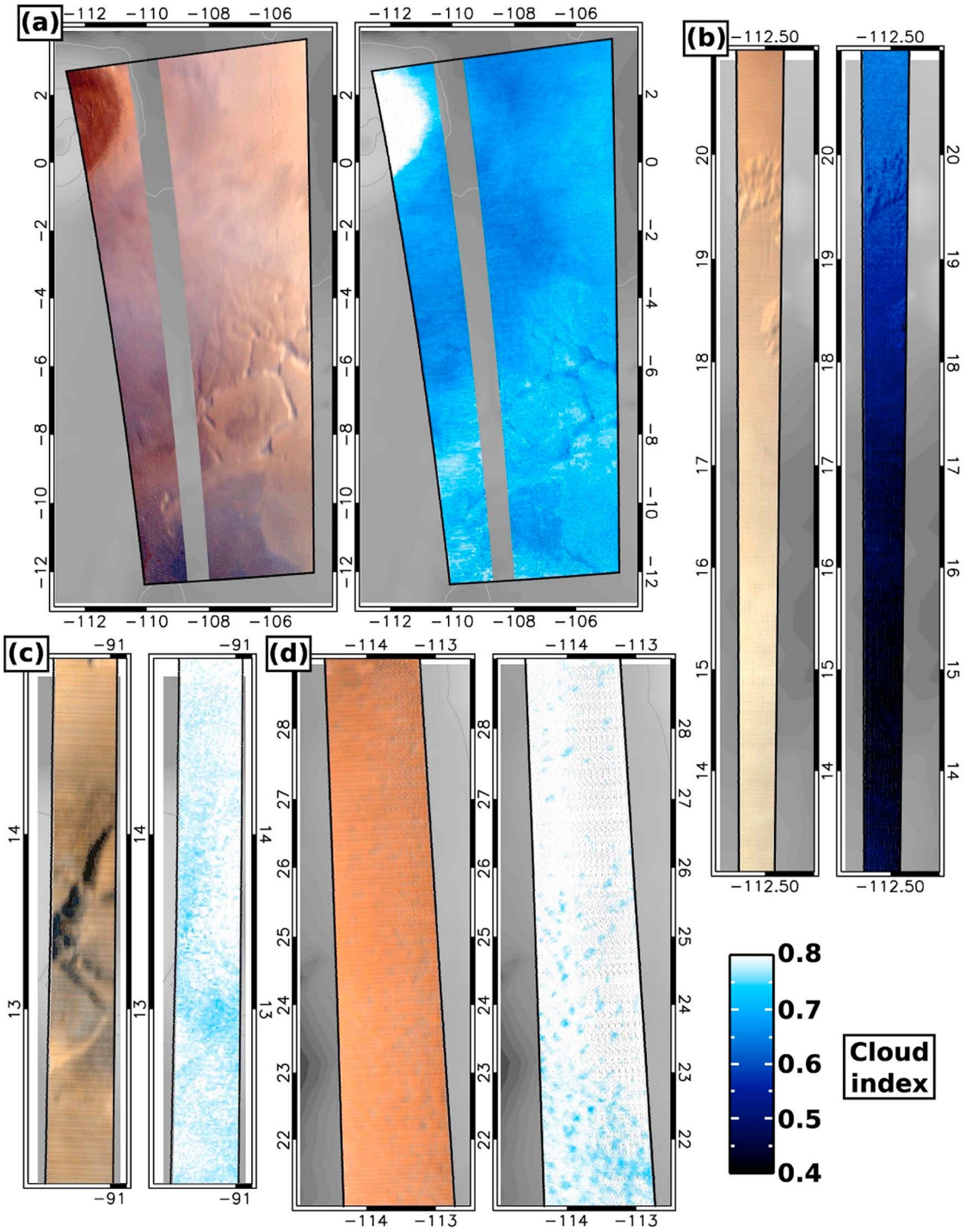

Figure 3. Selection of observations showing the four main types of clouds described in this paper (see section 3.5). For each observation, the visible channel image and the cloud index are shown. The blue shade reflects the strength of the 3.1 μm band, and is indicative of cloud formation (see section 3.1). (a) *Morning hazes* (L_s = 53.6°, LT = 8.5, orbit 563_3). (b) *Thick hazes* (L_s = 93.8°, LT = 16.5, orbit 891_5). (c) *Topographically controlled hazes* (L_s = 44.9°, LT = 13.4, orbit 5394_2). (d) *Cumulus clouds* (L_s = 115.3°, LT = 10.6, orbit 3514_1). The values of the cloud index are given in the lower right corner (see section 3.1).

mentioned before. *Thick hazes* are also found, especially north of Valles Marineris (red box) and around Pavonis Mons. Figure 3d is a detailed view of the cumulus clouds seen north of Pavonis Mons in Figure 2a. Lee waves structures are sometimes seen in hazes, as noticed early by *Briggs and Leovy* [1974] and *Kahn* [1984]. Shortly after mid-summer (L_s = 148°), around the same local time, all clouds have completely disappeared, as indicated by the red

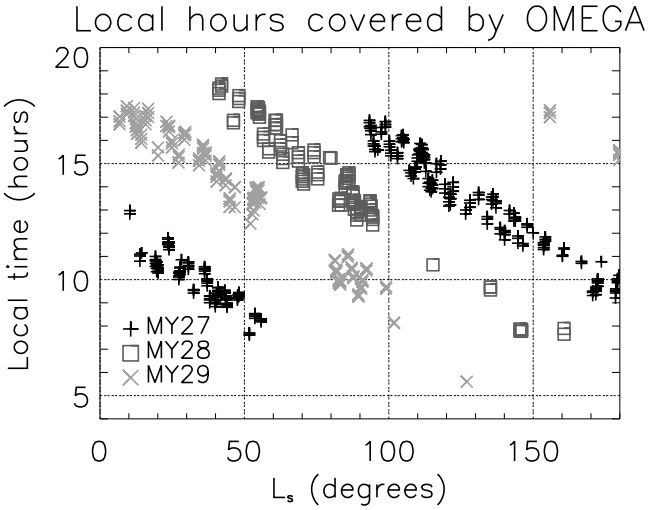

Figure 4. The solar longitude and local time of all the OMEGA observations analyzed in this paper. All the observations are acquired over the Tharsis plateau.

box of Figure 2d. The same evolution is observed in Figures 2c and 2e. The red box of Figure 2c indicates a region of thick hazes, observed at 10 PM and $L_s = 135°$. By $L_s \simeq 170°$, they have sublimated entirely (Figure 2e). Consequently, the decay of the aphelion cloud belt is sudden and happens around $L_s \simeq 150°$, in agreement with previous analyses.

3.4. Cloud Diurnal Variations

[27] The OMEGA data set offers many opportunities for diurnal comparisons of cloud properties. As seen in Figure 4, the $L_s = 0–30°$ period can be analyzed at two different local times, around 10 AM and 4 PM, for MY27 and 29, respectively. This corresponds to the two maps (a) and (c) of Figure 1. Over the $L_s = 30–60°$ period, three local times are available, 9 AM, 2 PM, and 5 PM, for MY27, 29, and 28, and the corresponding maps are given in Figures 1b, 1d and 1f. There is only one map for the $L_s = 60–90°$ period, shown in Figure 1e. Finally, the three remaining periods (90–120°, 120–150°, and 150–180°) were always covered at two different local times, and are given by Figures 2a–2b, 2c–2d and 2e–2f.

[28] *Early spring (L_s = 0–30°).* In the late mornings (11 AM) of early spring, no clouds are present (see the black box in Figure 1a), except some rare and extremely thin hazes that are not detected by the near-infrared channels, but discernable in the visible images. In the afternoon, around 5 PM, patchy haze forms over sloping regions, for example west of Ascraeus Mons and in Syria Planum (see the black box in Figure 1c).

[29] *Mid-spring (L_s = 30–60°).* In mid-spring of MY 27, OMEGA nicely covered the morning haze of Tharsis, as depicted in Figure 1b. This haze is shown in detail in Figure 3a, and has no discernable morphology. A few cumulus clouds, clustered over a dark area, are also seen in Echus Chasma at 8 AM (north of the third black box in Figure 1b). The evolution of the haze can be followed in the three black boxes that are common to Figures 1b and 1d. These boxes show an ubiquitous haze in Figure 1b at 8–10 AM, which vanishes in Figure 1d at 1–2 PM. Instead, a thin haze forms over the slopes of Pavonis Mons (left box), north of Valles Marineris (middle box) and near Lunae Planum (right box). This haze seems to be topographically controlled, as illustrated in Figure 3c where it forms over the slopes of Tharsis Tholus. The haze intensifies later in the afternoon. It is emphasized in the lower left black box common to Figures 1d and 1f, which indicates an increasing cloud index west of Pavonis Mons as we head through the afternoon (1 PM to 6 PM). The upper left boxes of Figures 1d and 1f show the region west of Alba Patera where cumulus clouds are seen at 1 PM (Figure 1d) and where a thick patchy haze forms later in the afternoon, at 6 PM (Figure 1f). Figure 1f also emphasizes the preferential location of clouds west of Lunae Planum (around 10°N and 90°W).

[30] *Late spring (L_s = 60–90°).* The early afternoon of late spring is characterized by *cumulus clouds* and *thick hazes*, as described in section 3.3. However, no diurnal comparisons can be made for this time period.

[31] *Early summer (L_s = 90–120°).* At the beginning of the afternoon, early summer is characterized by frequent cumulus clouds, which are sometimes accompanied by a thick and patchy haze (Figure 2a). Later in the afternoon, at 4 PM, a thick and ubiquitous haze forms north of Valles Marineris and in a triangle delimited by Olympus Mons and the Tharsis Montes (see Figure 2b). Comparing the black box in Figures 2a and 2b confirms that haze formation is intensified through the afternoon, and closer inspection reveals that cumulus clouds persist, even though they are hardly discerned in the haze. Figure 3b gives an example of haze which is especially thick, and whose opacity increases southward to a point where surface disappears in the visible channel.

[32] *Mid-summer (L_s = 120–150°).* When the decay period of the aphelion cloud belt starts ($L_s \sim 140°$), the early morning haze seems to persist at 8 AM, as indicated by the two black boxes at 112°W and 80°W in Figure 2c. However, it is less ubiquitous than mid-spring morning haze (see Figure 1b). Later in the morning and earlier in the season, at 10 AM, thick clouds are seen over the western flank of Ascraeus Mons (see the black box at 108°W in Figure 2c) and display a more cumuliform and patchy shape. Clouds completely disappear at noon, as seen when comparing the three black boxes in Figures 2c and 2d. Around 1 PM, they are not discernable anymore, except south of Syria Planum (under the second black box in Figure 2d), where thin cumulus clouds and lee waves persist. It is worth adding that afternoon clouds are seen around 75°W in Figure 2f at L_s = 156°. This suggests that clouds still form through the afternoon at the end of mid-summer.

[33] *Late summer (L_s = 150–180°).* Thin hazes are still visible in the morning at $L_s \sim 165°$, as seen in Figure 2e around 65°W. However, these hazes are not present later in the season. The only clouds that persist at the end of summer are located over Arsia Mons, where a thick haze forms through the afternoon, as indicated by the black box in Figures 2e and 2f. This reappearance of the cloud cover near Arsia Mons has also been reported by *Benson et al.* [2003] after $L_s = 140°$.

3.5. Summary

[34] The seasonal evolution observed by OMEGA is consistent with previous analyses, and consists of three main

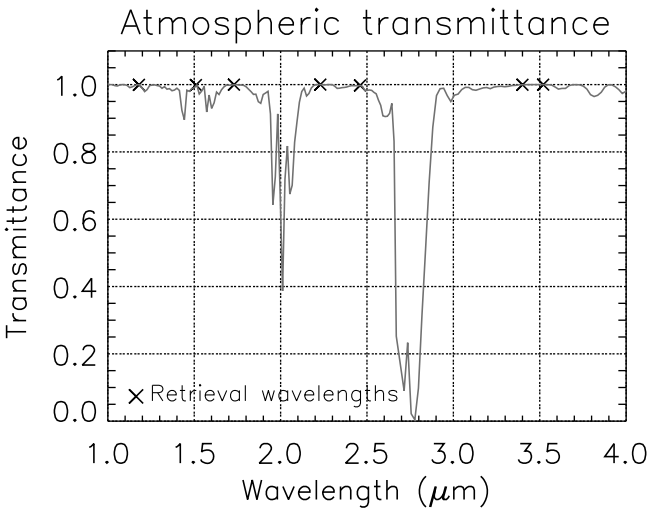

Figure 5. Transmittance spectrum of the Martian atmosphere. Retrieval wavelengths are located outside the main gaseous absorption bands (times symbols). Ad-hoc corrections for gases are therefore avoided, which conveniently reduces the number of problem parameters and resulting uncertainties.

periods. First, the appearance of thin hazes over the Tharsis plateau between $L_s \sim 20°$ and $L_s \sim 40°$. Then, the development of the aphelion clouds that culminates around $L_s = 100°$. And finally, the disappearance of the clouds around $L_s = 150°$.

[35] Four main types of clouds are distinguished, and their seasonal and diurnal evolution can be summarized as follows:

[36] 1. *Morning hazes* are found around 8 AM and are reported by OMEGA in mid-spring and mid-summer. They are probably remnants of fogs that form during the night. They dissipate before noon, and persist until $L_s \sim 165°$.

[37] 2. *Topographically controlled hazes* are observed at various local times, ranging from late morning to late afternoon. They seem to be present only in early spring and late summer.

[38] 3. *Cumulus clouds* begin to grow in mid-spring until mid-summer, and are often observed in the early afternoon, even though some are also observed in the morning. For example, one observation shows cumulus clouds at 8 AM over a particularly dark region of Echus Chasma.

[39] 4. *Thick hazes* form from mid-spring to mid-summer. They grow rapidly through the afternoon, and are especially abundant around $L_s = 100°$, in a region north of Valles Marineris and in a triangle delimited by the Tharsis volcanoes and Olympus Mons. They are the most opaque clouds found during the aphelion season over the Tharsis plateau.

4. Cloud Property Retrievals

[40] In this section, the particle size and visible opacity of the clouds are retrieved using the absorption bands of water ice. The retrieval method is described in section 4.1, and the retrieved properties are analyzed in section 4.2. The details of the uncertainty assessment can be found in Appendix A and in Table 3.

[41] Because of the difficulty in retrieving surface albedo and associated uncertainties, our retrieval method can only be applied to clouds whose visible opacity is larger than unity. Therefore, the present analysis of cloud properties is restricted to the *thick hazes* described in section 3.

4.1. Inversion Method

[42] The cloud property retrieval method (used in section 4.2) consists of retrieving cloud particle size and opacity by using the near-infrared absorption bands of water ice, which are mainly located near 1.5, 2 and 3.1 μm. When retrieving the properties of a given aerosol, one also has to pay attention to gaseous absorptions, which can significantly affect, or even prevent the retrieval. Figure 5 gives the transmittance spectrum of the Martian atmosphere when no aerosols are present. Many spectral regions are affected by gaseous absorptions and their reflectance cannot be directly used to retrieve the aerosol properties. The retrieval wavelengths are therefore chosen outside these gaseous bands, and indicated by times symbols in Figure 5. A typical cloud spectrum measured by OMEGA is represented in Figure 6 (dark grey), along with the fitted synthetic spectrum used for cloud property retrieval (times symbols). The location of the original cloud spectrum is indicated by the arrow in Figure 7. The retrieval wavelengths allow the measurement of cloud properties through the absorption band at 1.5 μm (1.18, 1.51, and 1.73 μm), the inflection on the edge of the 2 μm band (2.23 and 2.46 μm) and the wing of the 3.1 μm band (3.4 and 3.52 μm), as can be seen in Figure 6. The center of the 2 μm band is strongly affected by CO_2 and

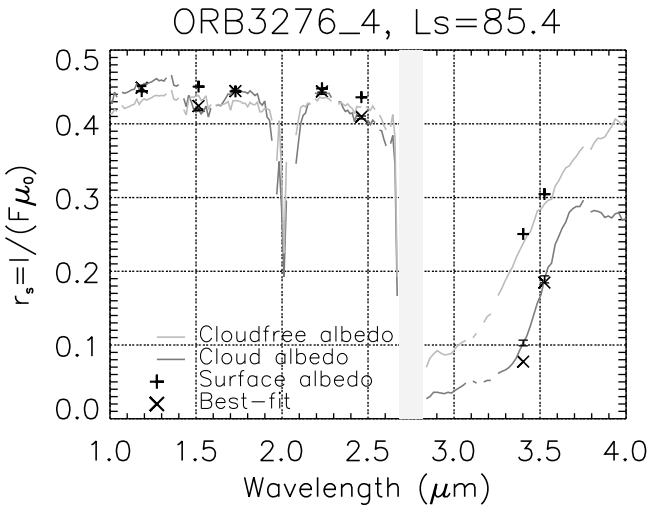

Figure 6. Example of fit obtained for a typical cloud (shown in Figure 7). The cloud-free and cloud spectra measured by OMEGA are shown in light and dark gray, respectively. The 1.5 μm water ice absorption band is clearly seen, whereas the 2 and 3.1 μm bands are reflected by the negative and positive slopes around 2.2 and 3.4 μm, respectively. Plus symbols show the surface albedo obtained after removing the contributions of scattering by the dust layer and thermal emissions. Times symbols represent the final best-fit. Instrumental 1-σ error is also given for the cloud spectrum, but can hardly be distinguished, except maybe in the L channel.

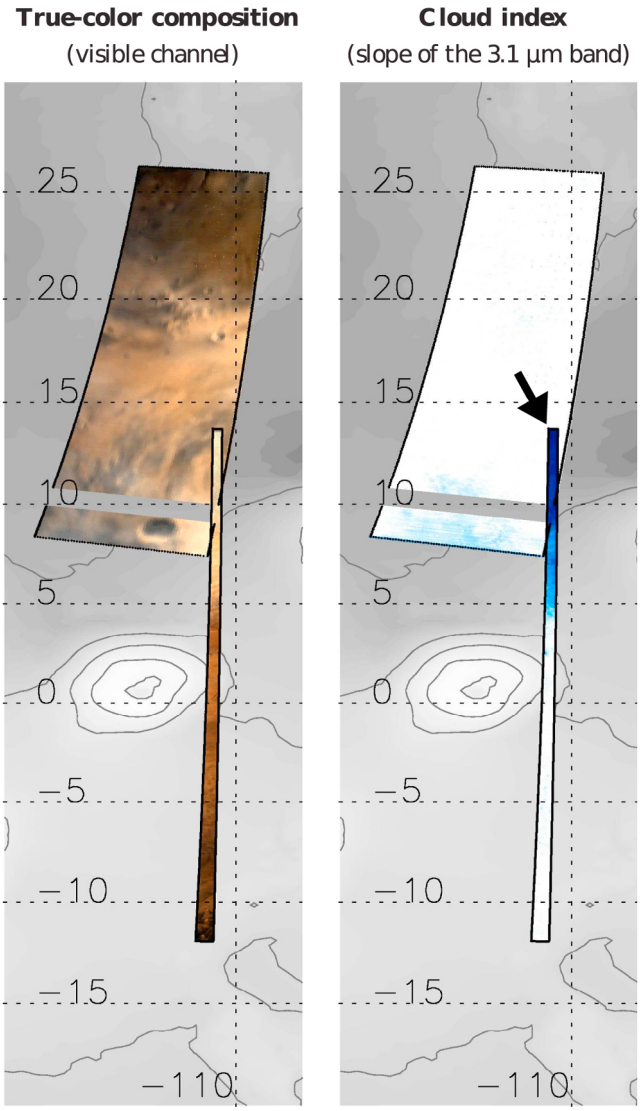

Figure 7. True-color composition and cloud index of the two orbits used in section 4.1 to describe the retrieval process. The blue shades in Figure 7, right, indicate the presence of water-ice clouds (see section 3.1 for more details on the cloud index). The wide orbit (3741_4) provides a cloud-free spectrum of the area where the retrieval is to be performed. The cloud spectrum is given by another orbit, which is the narrower orbit in the lower right corner (3276_4). The location of the retrieval is indicated by an arrow. Shaded colors in background are MOLA topography, and Pavonis Mons is in the center.

can even be used to retrieve surface pressure [*Forget et al.*, 2007; *Spiga et al.*, 2007]. This is why we only use the edge of the 2 μm band, the problem being sufficiently constrained by using the above mentioned wavelengths. We also avoid the water vapor absorption bands, located at 1.38, 1.9, and 2.6 μm [cf. *Encrenaz et al.*, 2005; *Maltagliati et al.*, 2008].

[43] All the computations described in this section are thus applied to these 7 reflectances, to finally retrieve cloud particle size and opacity. Figure 8 summarizes the main steps of the retrieval process and each step is described in the sections below.

4.1.1. Selection of the Cloud Spectrum

[44] The retrieval process starts with the selection of a cloud spectrum over which the retrieval is performed. First, another observation, acquired under clear conditions, must be available at the location of the cloud spectrum, as described in the next section. Then, the cloud must be sufficiently thick to allow the retrieval of its properties, mainly because of the uncertainty on the albedo of the surface (see Appendix A for more details). The visible opacity of the cloud has therefore to be larger than unity. As we discussed in section 3.1, this corresponds to a deep blue color and low value of the cloud index, which is used to select the appropriate cloud. Orbit 3276_4 is chosen as an example and represented in Figure 7. The figure gives a true-color view of the scene on the left and the cloud index on the right. Orbit 3276_4 overlaps a wider orbit (orbit 3741_4) where no clouds are detected.

4.1.2. Corresponding Cloud-Free Spectrum

[45] Once a cloud spectrum is selected, a reference spectrum, free of any cloud, must be found at the same location to compute the surface albedo. In most cases, it is impossible to find a cloud-free spectrum on the same orbit as that of the cloud spectrum, due to the large-scale and diffuse nature of the aphelion clouds, and the heterogeneity of the surface. That is why another observation, free of any cloud and covering the same region, has to be found and used to retrieve the albedo of the surface below the cloud. A synthetic cloud spectrum is then fitted to the observed cloud spectrum using the retrieved surface albedo as a lower boundary condition. The choice of a cloud-free spectrum is therefore crucial, and the following criteria are applied:

[46] 1. The difference in dust opacity at 0.88 μm between the two observations, estimated from simultaneous measurements by the Mars Exploration Rovers [*Lemmon et al.*, 2004], must be lower than 0.5;

[47] 2. The incidence angles of the two spectra must not differ by more than 40°, and pointing must not be in the anti-solar or specular directions;

[48] 3. Significant slopes must be avoided.

[49] The first criterion is related to uncertainties in the properties of the dust layer when dust opacity is high and typical of the perihelion season. Clouds form during aphelion when dust opacity is generally low. However, the cloud-free spectrum is often found during the perihelion, when the dust layer can reach significant opacity. When the difference in dust opacity between the two observations is larger than 0.5, it means that the cloud-free observation occurs during the period of peak dust activity. In this case, dust properties depart from the ones of the background dust assumed in our model (Gamma distribution of cylinders, axial ratio D/L=1, effective radius r_{eff} = 1.5 μm, ν_{eff} = 0.3; see section 4.1.4) and this results in a flawed assessment of the surface albedo.

[50] The second criterion results from the assumption of a Lambertian surface, which can differ from the real surface phase function, especially when surfaces are bright. Minimizing the difference between the two incidence angles and avoiding the anti-solar and specular directions is a way to reduce this uncertainty due to the Lambertian assumption.

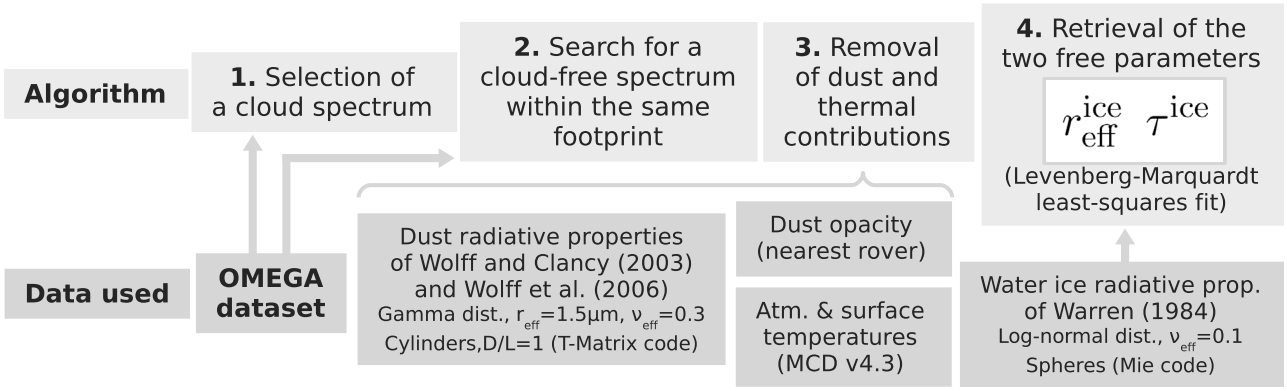

Figure 8. Summary of the retrieval method. The four main steps are given on top of the panel, and the data used to constrain the model parameters are at bottom. As indicated by steps 1 and 2, the retrieval method needs two overlapping orbits, with and without clouds. The cloud-free spectrum is used to compute surface albedo before retrieving the cloud properties. The contribution of the dust layer is taken into account via the opacity measurements of the MERs. Thermal contribution is also computed, based on the temperatures of the Mars Climate Database (MCD) v4.3 [*Forget et al.*, 1999; *Millour et al.*, 2008]. The radiative transfer is solved using the DISORT code of *Stamnes et al.* [1988], and the best fit is found with a Levenberg-Marquardt method.

[51] The last criterion ensures that there are no reflections on strong slopes, shadows, or registration problems and that the observation is consistent with the assumption of a flat surface made in the radiative transfer model.

4.1.3. Dust and Thermal Contributions

[52] Once the two spectra are selected, the cloud-free spectrum is used to compute surface albedo. Surface albedo is indeed the only quantity that does not significantly change from one observation to another (although decadal changes in surface albedo do occur due to dust transport, as described, for example, by *Fenton et al.* [2007]). Dust scattering and thermal emissions have to be removed from the cloud-free spectrum, and then replaced by their contributions at the time of cloud observation to perform the retrieval. This implies a good knowledge of the dust layer properties on the one hand, and of the surface and atmospheric temperatures on the other.

4.1.4. Dust Layer Properties

[53] Dust single scattering parameters are computed from the most recent refractive index of *Wolff et al.* [2009] using the T-Matrix code of M. Mishchenko [*Mishchenko et al.*, 1996] for a Gamma size distribution (r_{eff} = 1.5 μm, ν_{eff} = 0.3) of finite cylinders (D/L = 1 [cf. *Wolff et al.*, 2001]). A Henyey-Greenstein phase function is assumed. This is the closest match to the observed background properties and, even though these properties can change as dust particle size distributions evolve, we show in Appendix A that they are not a significant source of error, provided that the first criterion defined in section 4.1.2 is applied. Dust is assumed to be uniformly mixed, although its vertical distribution has almost no impact on the retrieved parameters.

[54] More uncertain is the dust opacity at the time and location of the two OMEGA observations. Fortunately, the Mars Exploration Rovers provide daily measurements of dust optical depth [*Lemmon et al.*, 2004] during the years of operation of Mars Express. Hence, the dust opacity at the time and location of the OMEGA observation can be deduced by scaling the contemporaneous opacity given by the closest of the two MERs to the altitude of the current footprint:

$$\tau_{\Omega} = \tau_{\mathrm{MER}} \exp^{-\frac{z_{\Omega} - z_{\mathrm{MER}}}{H}}, \tag{2}$$

with H the scale height, taken constant and equal to 10.8 km. We thus extrapolate the measurements of the MERs which can be thousands of km away by assuming that dust is uniformly mixed horizontally and vertically. As shown by *Vincendon et al.* [2009], this assumption is reasonable, although it introduces considerable uncertainty (this point is further discussed in Appendix A).

4.1.5. Atmospheric and Surface Temperatures

[55] Thermal emission by surface and atmospheric constituents can be neglected in the C channel. For example, the ratio of the solar irradiance at 1.52 AU to the one emitted by the Martian surface at 290 K (assuming an emissivity of 1) is equal to $\sim$3000 at 2.56 μm, which is the largest wavelength used for our inversion in the C channel. However, this ratio plummets by 2 order of magnitude for the two wavelength of the L channel, being equal to $\sim$19 and $\sim$12 at 3.4 and 3.52 μm, respectively. It is therefore necessary to account for thermal emission, primarily by the surface as the atmosphere is too cold to significantly impact the OMEGA spectrum. Surface temperatures as well as atmospheric temperature profiles are extracted from the Mars Climate Database v4.3 (MCD) [*Forget et al.*, 1999; *Millour et al.*, 2008] and interpolated in time, given the large dependence of surface temperature to the local time of observation (the related uncertainty is discussed in Appendix A). The surface emissivity is simply defined as $\epsilon = 1 - A_N$.

4.1.6. Surface Albedo Retrieval

[56] Once temperature and dust opacity are specified, the spectral albedo of the surface is retrieved by computing for each wavelength the root of the function $f(A_s) = r_{s,\Omega} - r_{s,\mathrm{model}}(A_s)$, which is the difference between the observed cloud-free reflectance and the reflectance simulated by the

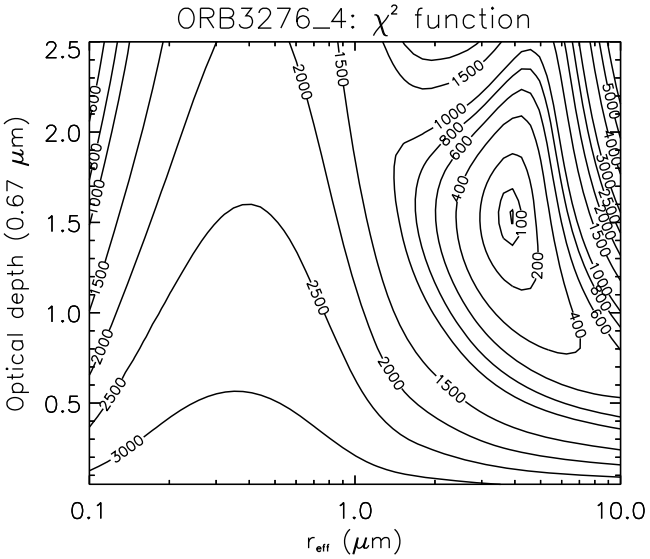

Figure 9. Example of χ^2 function used in the cloud property retrieval of Figure 7, and showing the function minimum close to $r_{\text{eff,ice}}$ = 4 μm and τ_{ice} = 1.5. A shallower minimum is seen in the upper left corner of the plot, and corresponds to an extremely thick cloud of submicron particles. The minimization algorithm is initialized with large particles to avoid this local minimum.

DISORT radiative transfer code. The surface albedo (A_s) used by DISORT is the free parameter of the root-finding algorithm, and dust opacity and surface temperatures are held constant. The root-finding algorithm is based on the Müller's method and provided by the FX_ROOT function of IDL. This method is efficient and justified by the monotonicity of the $f(A_s)$ function.

[57] The retrieved surface albedo is shown in Figure 6. The initial cloud-free spectrum is given in light gray, and the seven reflectances computed after removing the dust layer and thermal contributions are represented by the plus symbols. The local dust opacity at 0.88 μm deduced from the nearest rover measurement is equal to 0.42, and the surface is relatively cold (218 K) because of the early morning hour (~8 AM). The original reflectance spectrum is darker than the retrieved surface albedo because the addition of atmospheric dust tends to darken the surface in this case where the surface is relatively bright. The surface temperature is too low to have a notable impact on the L channel reflectance.

4.1.7. Retrieval Algorithm

[58] Once the surface albedo is known, the retrieval procedure can be performed using the observed cloud spectrum. Dust opacity and surface temperature deduced at the time of the cloud observation are used, instead of the ones used earlier to retrieve surface albedo. In our example, a dust opacity of 0.2 is deduced from the nearest rover measurement and surface temperature is equal to ~264 K, the latter having now a substantial impact on the reflectances of the L channel.

[59] The synthetic cloud spectrum is then fitted to the observed cloud spectrum using a least squares minimization. The minimization algorithm is provided by the MPFIT routine of *Markwardt* [2009] (http://purl.com/net/mpfit), which is based on the non-linear least squares fitting program of *Moré et al.* [1984] called MINPACK. It follows the Levenberg-Marquardt method and computes the covariance matrix, from which the uncertainty in the two free parameters is calculated. This uncertainty only results from instrumental uncertainties in the measured radiance. Errors resulting from inaccurate model parameters are assessed separately (see section A2). The two free parameters are the effective radius of ice crystals $r_{\text{eff,ice}}$ and the cloud optical depth τ_{ice} at 0.67 μm. The statistical χ^2 function is weighted by the variance of measured reflectance (defined in section A1) and is given by:

$$\chi^2 = \sum_i \left(\frac{r_{s,\Omega}(\lambda_i) - r_{s,\text{model}}(\lambda_i)}{\sigma_\Omega(\lambda_i)} \right)^2. \quad (3)$$

[60] The DISORT code used to create the synthetic cloud spectrum is run with 16 streams. The water ice optical indices are those from *Warren* [1984]. Single scattering parameters are deduced from Mie theory for a range of spherical particles of varying effective radius. A Henyey-Greenstein phase function is used, and the distribution follows a lognormal distribution of effective variance $\nu_{\text{eff}} = 0.1$. This low value is chosen to be representative of the narrowing of the size distribution due to the rapid growth of the water ice particles [*Colaprete et al.*, 1999; *Michaels*, 2008]. Uniform mixing of cloud particles is assumed, from 25 km upward. The uncertainties in the cloud altitude and effective variance of the size distribution have a negligible impact on the retrieval, as mentioned in Appendix A.

[61] The χ^2 function that corresponds to our example is shown in Figure 9, in which the minimum near $r_{\text{eff,ice}}$ = 4 μm and τ_{ice} = 1.5 clearly appears. The fit is more sensitive to particle size than optical depth and the overall convergence is fast, due to the steepness of the χ^2 function. A secondary and shallower minimum is present for very thick clouds composed of submicron particles (upper left corner of Figure 9). There the quality of the fit is poor. Based on previous studies of cloud properties [*Curran et al.*, 1973; *Clancy et al.*, 2003; *Wolff and Clancy*, 2003; *Glenar et al.*, 2003], we do not expect such clouds to actually exist, at least at this time and location. Consequently, the minimization algorithm is initialized with a particle size of 10 μm and a cloud opacity of 2 to prevent the algorithm from falling in this secondary minimum. During the minimization, the χ^2 function drops by 2 orders of magnitude, more exactly from 7800 to 78. The final χ^2 value is often much larger than unity because of the high precision of the instrument, which introduces a relatively low variance σ_Ω in equation (3) (the mean instrumental error is about 0.2%, see section A1). It is also due, in some cases, to the difficult fit in the L channel (see Figure 6).

[62] The result of the minimization is $r_{\text{eff,ice}}$ = 3.9 ± 0.3 μm and τ_{ice} = 1.5 ± 0.09.

4.2. Retrieved Cloud Properties

4.2.1. Cloud Selection

[63] As mentioned earlier, our retrieval method is only applicable to clouds whose visible opacity is near unity. Consequently, we are only able to retrieve the properties of

Table 1. List of All the Retrievals Performed Over the Tharsis Plateau (See the Map of Figure 10) for the L_s = 85.4–121.4° Period[a]

	Orbit	Lon (°)	Lat (°)	L_s (°)	LT (h)	z (km)	i (°)	e (°)	$r_{eff,i}$ (μm)	$\sigma_{reff,i}$ (μm)	τ_i	σ_{τ_i}	WIC (pr.μm)	σ_{WIC} (pr.μm)	Δi (°)	$\Delta\tau_d$
1	0887_5	−80.0	8.8	93.3	16.9	−0.6	69.9	5.7	5.4	$^{+1.1}_{-0.8}$	1.0	$^{+0.12}_{-0.12}$	3.3	$^{+0.9}_{-1.1}$	41.8	0.24
2	0891_5	−112.6	10.8	93.8	16.5	2.5	68.8	2.5	5.0	$^{+0.4}_{-0.3}$	1.7	$^{+0.09}_{-0.09}$	5.2	$^{+0.6}_{-0.6}$	39.8	0.21
3	0898_5	−80.5	3.7	94.7	15.8	−0.8	71.2	2.3	4.7	$^{+0.5}_{-0.4}$	1.3	$^{+0.09}_{-0.10}$	3.7	$^{+0.6}_{-0.6}$	40.6	0.43
4	0902_5	−113.6	16.7	95.2	15.6	2.2	64.6	2.7	4.9	$^{+0.7}_{-0.5}$	1.2	$^{+0.10}_{-0.11}$	3.6	$^{+0.7}_{-0.8}$	20.7	0.19
5	0920_5	−82.0	8.2	97.4	16.4	0.0	66.3	1.5	4.7	$^{+0.7}_{-0.5}$	1.2	$^{+0.10}_{-0.11}$	3.5	$^{+0.7}_{-0.8}$	31.3	0.22
6	0946_6	−117.0	1.3	100.7	15.6	5.2	65.7	0.4	4.7	$^{+1.3}_{-0.8}$	0.8	$^{+0.13}_{-0.13}$	2.3	$^{+0.8}_{-1.0}$	38.9	0.34
7	1012_6	−122.2	6.7	109.1	14.8	4.5	53.4	0.3	3.4	$^{+0.4}_{-0.3}$	1.4	$^{+0.10}_{-0.10}$	2.9	$^{+0.5}_{-0.5}$	14.4	0.22
8	1012_7	−122.2	−2.2	109.1	14.8	5.0	58.0	0.3	5.1	$^{+1.8}_{-1.2}$	0.7	$^{+0.15}_{-0.11}$	2.2	$^{+0.9}_{-1.2}$	22.0	0.21
9	1023_6	−123.1	16.1	110.5	15.6	1.0	47.8	0.1	2.3	$^{+0.6}_{-0.4}$	1.0	$^{+0.18}_{-0.19}$	1.3	$^{+0.5}_{-0.6}$	15.4	0.40
10	1034_6	−124.0	7.5	111.9	15.4	4.6	49.8	0.2	2.2	$^{+0.3}_{-0.2}$	1.3	$^{+0.12}_{-0.13}$	1.7	$^{+0.4}_{-0.4}$	25.5	0.29
11	1107_1	−97.2	16.9	121.4	13.5	2.6	35.2	0.1	2.8	$^{+0.3}_{-0.3}$	1.4	$^{+0.10}_{-0.11}$	2.3	$^{+0.4}_{-0.5}$	1.0	0.26
12	1107_2	−97.3	−13.6	121.4	13.7	6.6	51.9	0.3	2.4	$^{+0.4}_{-0.3}$	1.2	$^{+0.12}_{-0.13}$	1.7	$^{+0.4}_{-0.5}$	29.1	0.28
13	3276_3	−110.5	15.3	85.4	14.2	2.0	29.9	0.4	4.8	$^{+0.7}_{-0.5}$	1.1	$^{+0.11}_{-0.11}$	3.3	$^{+0.7}_{-0.8}$	0.4	0.27
14	3276_4	−110.5	13.3	85.4	14.4	2.0	30.9	0.3	3.9	$^{+0.3}_{-0.3}$	1.5	$^{+0.09}_{-0.09}$	3.5	$^{+0.5}_{-0.5}$	8.0	0.23

[a]The altitude of the surface relative to the areoid and the observing geometry are given for each observation. Measured ice particle size and cloud visible opacity are listed, along with the Water Ice Column in pr.μm (WIC, see section 4.2.1). Corresponding 1-σ errors are also given. The two last columns indicate the difference in incidence and dust opacity at 0.88 μm between the cloud-free and cloud spectra. Ice particle sizes are plotted as a function of L_s and local time in Figure 11.

thick hazes. The error on the measured particle size and cloud opacity becomes too large when considering thin clouds such as *morning hazes*, *cumulus clouds* or *topographically controlled hazes.* The following measurements will be thus biased toward high opacity values when compared to previous works.

[64] We select the observations showing the thickest hazes, which mainly occur around L_s = 100°, and look for conditions favorable to the retrieval of their properties. These conditions are listed in section 4.1.2 and the selection mainly consists of finding a cloud spectrum that overlaps a cloud-free spectrum acquired with a similar geometry, both spectra being made under low dust load conditions and over a relatively flat surface. The flanks of the volcanoes are avoided and we rather focus on the surrounding plateaus.

[65] A map of the selected observations is shown in Figure 10, along with the locations of previous retrievals made in the same region and time period by *Zasova et al.* [2001] (IRIS/Mariner 9, triangles) and *Wolff and Clancy* [2003] (TES/MGS, diamond). The corresponding results are listed in Table 1 for OMEGA, and in Table 2 for IRIS and TES. All the observations fall in the L_s = 85.4–121.4° time period, and occur between 1 PM and 5 PM. They were all acquired in MY27, except observations #13 and 14, which correspond to MY28. The retrieved ice particle size and cloud opacity are used to compute the Water Ice Column (WIC), which is also reported in Table 1.

Table 2. Retrievals of Ice Particle Size and Cloud Opacity at Visible Wavelengths (Shown in Red in Figure 10) Performed Over the Same Region and in the Same Time Period as in Our Study[a]

	Lon (°)	Lat (°)	L_s (°)	LT (h)	$r_{eff,i}$ (μm)	$\sigma_{reff,i}$ (μm)	τ_i	$\sigma_{\tau i}$
1	−117.1	13.2	98.0	15.4	2.0	±0.5	0.46	……
2	−117.0	12.7	98.0	15.4	2.0	±0.5	0.46	……
3	−114.2	21.9	98.0	16.4	3.0	±0.5	0.48	……
4	−100.1	14.6	114.9	14.0	3.2	±0.8	0.31[b]	±0.04[b]

[a]The three first measurements come from a reanalysis of the IRIS/Mariner 9 data set performed by *Zasova et al.* [2001]. The last measurement was made with TES/MGS by *Wolff and Clancy* [2003].

[b]Original values at 12.1 μm are 0.23 and 0.03, respectively.

[66] The WIC in precipitable micrometers (pr.μm) can be calculated by assuming that $\tau = N\sigma_g Q_{ext}$, where τ is the total cloud optical depth, N the number of ice particles per m^2, σ_g the average area of the geometric projection per particle and Q_{ext} the particle extinction efficiency. The WIC in pr.μm can then be expressed:

$$\mathrm{WIC} = \int_0^\infty N\frac{4}{3}\pi r^3 n(r)\mathrm{d}r = \frac{4}{3}Nr_{\mathrm{eff}}\sigma_g = \frac{4}{3}\frac{\tau r_{\mathrm{eff}}}{Q_{\mathrm{ext}}}, \qquad (4)$$

where $n(r)$ is a lognormal distribution (ν_{eff} = 0.1), r_{eff} the effective radius of the distribution in μm and where Q_{ext} varies as a function of the ice particle size. The error on the WIC can be directly deduced from the errors on $r_{eff,ice}$ and τ_{ice}, and is also given in Table 1.

4.2.2. Spatial Description of the Cloud Properties

[67] The retrievals are mainly located in the triangle formed by Olympus Mons and the Tharsis Montes (in the upper left part of Figure 10). Three other retrievals are located in Echus Chasma (around 5°N–80°W), another one north east of Ascraeus Mons (#11), and a last one in Syria Planum (#12).

[68] The largest cloud index is found in a region west of Ascraeus Mons. The corresponding retrievals (#2, 4, 13 and 14) indicate particle sizes of 4–5 μm and a visible opacity of 1.1–1.7. The IRIS/Mariner 9 retrievals of *Zasova et al.* [2001] were carried out in the same region (see the red triangles in Figure 10 and retrievals #1, 2, 3 in Table 2) and

Table 3. Uncertainties on the Retrieved Parameters for Different Ice Particle Sizes and a Cloud Opacity of Unity[a]

$r_{eff,ice}$ (μm)	τ_{ice}	Error on $r_{eff,ice}$ (μm)	Error on τ_{ice}
2.5	1.0	$^{+0.7}_{-0.4}$	$^{+0.19}_{-0.16}$
4.0	1.0	$^{+0.9}_{-0.6}$	$^{+0.15}_{-0.13}$
6.3	1.0	$^{+1.5}_{-1.0}$	$^{+0.12}_{-0.13}$
8.6	1.0	$^{+1.8}_{-1.5}$	$^{+0.09}_{-0.13}$

[a]The uncertainties come from instrumental errors, and from errors on surface albedo and temperature. Uncertainty on ice optical indices may result in a systematic bias toward lower ice particle sizes which is not shown in the table (see the details in Appendix A).

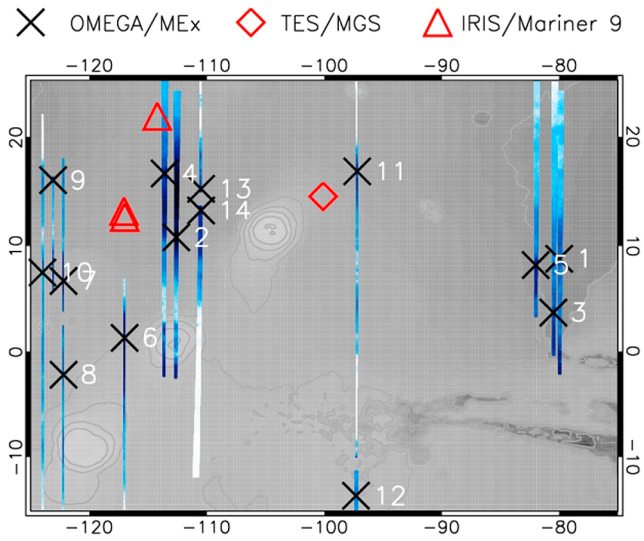

Figure 10. Map showing the location of the cloud property retrievals, which are listed in Table 1. Also represented in red are IRIS and TES retrievals (see Table 2) that were performed by *Zasova et al.* [2001] and *Wolff and Clancy* [2003], respectively. The cloud index map corresponding to each retrieval is also shown. A focus is made on the peak of the cloud season, around 100° of L_s. Solar longitude thus ranges from L_s = 85.4° to L_s = 121.4°. The analyzed spectra (times symbols) were acquired at various hours, and the retrieved particle sizes are shown as a function of L_s and local time in Figure 11.

indicate particle sizes of 2–3 μm. Given the size of the IRIS footprints (~200 km), these particle sizes are representative of the whole region, and can be expected to be lower than the ones retrieved by OMEGA, which are limited to the thickest clouds. This region has also been extensively observed by *Clancy et al.* [2003], who measured particle sizes of 2.5–4.5 μm (see Figure 18 therein) and categorized these clouds as "type 2" clouds.

[69] The cloud optical depth at 0.4 μm was retrieved by *Benson et al.* [2003] using MOC/MGS. The values they reported in the Ascraeus Mons region can be directly compared to our measurements at 0.67 μm without significant error. They range from 0.1 to 1.36 and are thus consistent with our retrievals. The maximum particle size and opacity observed by OMEGA are equal to 5 μm and 1.7, respectively, with an error of less than 10%. They are found in late afternoon (LT 16.5) on orbit 891_5 (Figure 3b). Ice particle sizes are also especially large west of Pavonis Mons (see Figure 10, retrievals #6 and 8), and in Echus Chasma (#1, 3 and 5), where they are close to 5 μm. The retrieved opacities are equal to 0.7–0.8 west of Pavonis Mons and 1–1.3 in Echus Chasma. These values are in agreement with the observations of *Benson et al.* [2003], who found opacities ranging from 0.16–1.3 for Pavonis Mons and 0.04–1.1 for Valles Marineris. All these regions are part of wider areas of intense cloud formation, mainly located west of Ascraeus and Pavonis Mons, and north of Valles Marineris [see, e.g., *Smith*, 2004, Figure 16].

[70] In these regions of thick clouds, the measured WIC is mostly equal to 2–3.5 pr.μm, with an especially high value of 5.2 pr.μm for orbit 891_5. *Benson et al.* [2003] measured a WIC of 0.15–2.1 pr.μm for Ascraeus Mons, 0.25–2 pr.μm for Pavonis Mons and 0.07–1.7 pr.μm for Valles Marineris, in agreement with *Mateshvili et al.* [2007] who observed a WIC of 1.35–1.8 pr.μm. Our values are therefore higher for reasons explained at the end of this section.

[71] Further away from the Tharsis volcanoes, over Ulysses Fossae (10°N–125°W), particle sizes are smaller than near the volcanoes, and equal to 2–3 μm (orbits #7, 9 and 10). The corresponding WIC ranges from 1.3 to 2.9 pr.μm.

[72] The last two observations were made at the same time, in the northeast of Ascraeus Mons (#11) and in Syria Planum (#12). Interestingly, *Wolff and Clancy* [2003] measured the cloud properties in a nearby area, at about the same L_s and local time (see the red diamond in Figure 10 and retrieval #4 in Table 2). The TES particle size of 3.2 μm is close to our value of 2.8 μm, whereas the TES opacity of 0.31 is much lower than the OMEGA opacity of 1.4. Indeed, our measurements focus on high opacity clouds, which is not the case of TES measurements (see section 4.2.1). Finally, the cloud properties in Syria Planum are similar to those near Ascraeus Mons, despite the distance between the two observations.

[73] In summary, cloud particle sizes are in agreement with previous analyses, and range from 2.2 to 5.4 μm. These clouds probably correspond to the type 2 clouds identified by *Clancy et al.* [2003]. Opacities are in agreement with *Benson et al.* [2003], even though our opacities are biased toward higher values due to the data selection process. The WIC ranges from 1.3 to 5.2 pr.μm, and is higher than previously reported by *Benson et al.* [2003] and *Mateshvili et al.* [2007]. It is probably due to the high opacity values, and also to the use of the true r_{eff} in the calculation of the WIC (see equation (4)). Indeed, a constant size of the ice particles was assumed in both studies [see *Benson et al.*, 2003, section 3.4; *Mateshvili et al.*, 2007, section 5.2.4]. Given the high opacity of the clouds in our study, the WIC we measure is probably close to the maximum values we can find in this region.

4.2.3. Seasonal and Diurnal Trends

[74] The seasonal and diurnal evolution of cloud properties is essential for understanding the cloud formation process. We therefore looked for variations in cloud properties as a function of L_s and local time. Care must be taken in interpreting these variations because L_s and local time are not independent, as they are both linked to the spacecraft orbit. It is illustrated by Figure 4, where we clearly see the decrease in local time as a function of L_s.

[75] Figure 11 shows the variation in $r_{eff,ice}$ as a function of L_s (Figure 11a) and local time (Figure 11b) for all orbits analyzed in this study. Previous measurements by *Zasova et al.* [2001] and *Wolff and Clancy* [2003] are also represented in red. No discernable trend is observed when considering all particle size measurements. However, there are two distinct groups of particles. A first group of 5 measurements, represented in blue, includes particles ranging in size from 2 to 3.5 μm. The second group, in black, is characterized by particles that are larger and about 5 μm in size. All the measurements of the first group are located in regions of reduced cloud cover (see Figure 10), whereas retrievals of the second group are done in the thickest clouds, i.e. near the Tharsis volcanoes and north of Valles Marineris. Therefore a

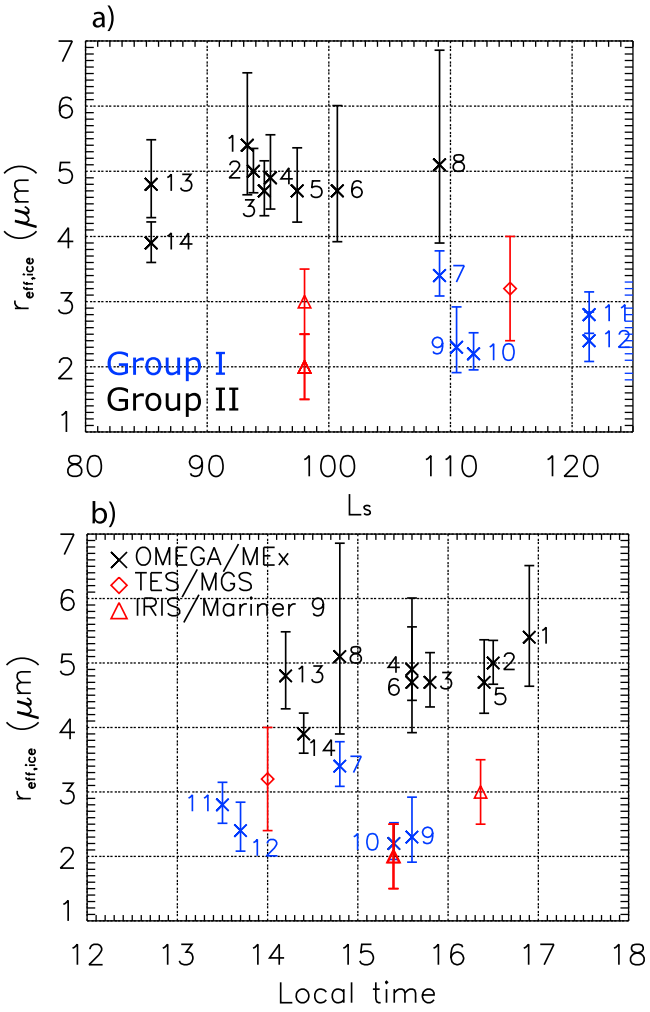

Figure 11. Retrieved ice particle size as a function of (a) L_s and (b) local time. Earlier measurements made by *Zasova et al.* [2001] (IRIS, red triangles) and *Wolff and Clancy* [2003] (TES, red diamond) in the same region are shown for comparison (see Table 2). The estimated 1-σ errors are represented and also given in Table 1. The location of all retrievals is represented in Figure 10. Two groups can be distinguished: a group of small particles (2–3.5 μm, in blue), and another group of large particles (~5 μm, in black), each group corresponding to different regions. Among the second group, particle size seems to be constant over L_s and local time.

difference in particle size seems to exist between the core and the periphery of the cloud belt. The previous measurements of *Zasova et al.* [2001] and *Wolff and Clancy* [2003], which are represented in red in Figure 11, would then belong to the cloud belt periphery.

[76] Interestingly, all the measurements refer to thick clouds, and there is no particular trend in opacity between the periphery and the core of the cloud belt. The distinction between the two groups seems to result from a difference in particle size alone.

[77] In the second group, particle sizes appear to be quite constant over L_s and local time, and remain close to 5 μm. For example, retrievals #2 and 13, which are done in the same region and at the same season for MY27 and 28, are more than two hours apart but present the same particle size. This suggests that a threshold size is reached over the course of a day. This threshold is not an artefact of our retrieval method, as larger particles would result in deeper absorption bands. Still, this phenomenon remains to be confirmed, as a robust conclusion would require a larger data set.

5. Interpretation

[78] In this section, the results of both the mapping and property retrieval of aphelion clouds are interpreted in the light of the meteorological conditions of the Tharsis region. The origin of the four cloud types is discussed in section 5.1, whereas the spatial variations in the retrieved cloud properties are considered in section 5.2.

5.1. Cloud Cover Evolution

[79] *Morning hazes* are present during spring and summer and dissipate by noon. Later in the morning, clouds start to form on the western flanks of the Tharsis volcanoes. During the afternoon and from mid-spring to mid-summer, *thick hazes* form, and sometimes present a patchy and cumuliform shape, which is hard to distinguish given the narrow swath of OMEGA.

[80] These diurnal variations seen by OMEGA are consistent with the early analyses of the Viking Orbiters. A first study by *Hunt et al.* [1980] reported, in the region of Ascraeus Mons, the evolution from a "pervasive fog" at LT = 5.5–7.3 to well developed clouds at LT = 11.2 for L_s = 121.5°. During the L_s = 0–90° period, *Christensen* [1998] and *Tamppari et al.* [2003] also noticed in the IRTM data an homogeneous haze between 8 AM and 10 AM, followed by minimum cloud cover at noon and by the appearance of more localized clouds during the afternoon.

[81] OMEGA comprehensively covered the morning haze during MY27 (see Figure 1b) and provides a detailed view of its spatial distribution. Its formation seems to be favored in regions of low thermal inertia and high surface albedo (compare Figure 1b with the maps of *Putzig et al.* [2005] and *Christensen et al.* [2001]), where we expect the lowest nighttime temperatures to occur.

[82] *Topographically controlled hazes* are only seen in early spring and late summer. In the aphelion cloud seasons, these are the periods when temperature and water vapor content are the least favorable to cloud formation. Consequently, these thin clouds (see Figure 3c) might form only in regions of extreme anabatic winds [*Michaels et al.*, 2006; *Spiga and Forget*, 2009], their development being limited by the difficulty to reach saturation. They might represent the early and late stages of *thick hazes* that appear from mid-spring to mid-summer and have the same dynamical origin.

[83] OMEGA also gives insight into the spatial and time distribution of *cumulus clouds*, that often grow in the early afternoon from mid-spring to mid-summer. This is the time of the day when surface temperature is the highest, and the time of the year when atmospheric temperature is the lowest. This corresponds to an optimal time when the boundary layer is the most active and when the saturation altitude is the lowest. This suggests that cumulus clouds originate from shallow convection, when water vapor transported upward

by convection is able to reach saturation altitude. This hypothesis has been examined by *Michaels and Rafkin* [2004], who compared MOC images of such cumulus clouds to Large Eddy Simulation (LES) results. The cumulus cloud spatial distribution compares well with the distribution of the strongest updrafts, and their altitude corresponds to the top of the convective boundary layer. Moreover, boundary layer depth increases with decreasing surface pressure, as explained by *Spiga et al.* [2010], and can almost reach 10 km over the Tharsis plateau. This corresponds to the altitude at which saturation can be reached, as measured for example by *Clancy et al.* [1996, Figure 3]. The increased thickness of the boundary layer over the Tharsis plateau would explain why the formation of cumulus clouds is favored in this region. Further spectral analyses of cumulus clouds at higher spatial resolutions are however required to confirm their convective origin.

[84] Interestingly, cumulus clouds are persistent south of Alba Patera and Valles Marineris, whereas they become hidden by thicker clouds in the other regions. For example, the orbits indicated by the red box in Figure 2a, which were acquired at 1 PM and $L_s = 90°$, clearly show this transition from *thick hazes* to *cumulus clouds* as we cross Valles Marineris and show many areas where both types coexist. Type 1 clouds were observed by TES at same season and local time and *Clancy et al.* [2003] described them as being "prevalent at mid southern latitudes during the aphelion season". Their Figure A1 clearly emphasizes the transition from type 1 to type 2 clouds as we cross the equator. They also mentioned that "the two ice types (may) coexist at the boundaries of the aphelion cloud belt", and that "the microphysical transition from type 1 ice to type 2 ice (may be) fairly continuous." Consequently, type 1 and type 2 clouds might correspond to the *cumulus clouds* and *thick hazes* identified in this study. Their distinct formation processes would explain the microphysical differences reported by *Clancy et al.* [2003]. This conclusion needs to be confirmed by checking the size of the particles in cumulus clouds, which are too thin to be characterized by OMEGA.

[85] The *cumulus clouds* are excellent indicators of local meteorological conditions. A lot could be learned about the Mars water cycle and cloud microphysics from examining their properties and trying to predict them accurately using multiscale climate modeling.

5.2. Cloud Microphysical Properties

[86] We only analyzed the properties of *thick hazes* and reached two main findings. First, there is a difference in particle size between what we called the "core" of the cloud belt and its "periphery". Secondly, in the core of the cloud belt, there seems to be no large change in cloud properties over season or local time.

[87] There are three main factors controlling the formation of the cloud belt and they all interact at various scales. The first factor is the availability in water vapor. The highest WIC measured in our study is 5.2 pr.μm, and represents approximately a third of the water vapor column found in these regions [*Smith*, 2004; *Fedorova et al.*, 2006]. Water vapor is thus in excess and the variations in the amount of water vapor brought by the atmospheric circulation do not have a strong impact on cloud formation. This explains why there is no apparent link between the periods of cloud development and those of water vapor injection [*Pearl et al.*, 2001; *Smith*, 2004]. The second factor is temperature, and the cloud belt is made possible by low aphelion temperatures, as many studies pointed out [*Clancy et al.*, 1996; *Richardson et al.*, 2002]. The third factor is atmospheric circulation. The regions west of the Tharsis Montes and north of Valles Marineris experience strong regional winds during summer solstice, which also control the formation of the cloud belt. As noticed by *Hunt et al.* [1980], this regional circulation changes at $L_s = 150°$, and could play a role, along with temperature, in the decay of the cloud belt.

[88] At finer scales, the difference in cloud properties between the core and the periphery of the cloud belt could be explained by this third factor, especially by the diurnal wind variations imposed by topography. Clouds are particularly developed in regions of strong anabatic winds, which are favored by the topographical slopes and the low thermal inertia of the Tharsis plateau [*Hunt et al.*, 1980]. All the retrievals performed in the core of the cloud belt are located in sloping regions, near Lunae Planum and west of Ascraeus and Pavonis Mons. The regions west of the Tharsis Montes and Olympus Mons have been studied by *Michaels et al.* [2006] using mesoscale modeling. The clouds in these regions are found to result from the interaction between anabatic winds and gravity waves induced by the volcanoes. They are created on the flanks of the volcanoes, in a "dynamically maintained region of sharply depressed temperature (up to 10 K deviation)" [*Michaels et al.*, 2006, p. 2, para. 10]. They grow rapidly and reach particle sizes of $r_{eff} \simeq 8$ μm. Once formed, ice crystals are carried aloft by large scale circulation, and leave the parcels where they formed.

[89] Apart from the three retrievals near Lunae Planum, all the measurements that indicate high particle sizes (second group in Figure 11) correspond to the location of the large particle clouds predicted by *Michaels et al.* [2006]. The persistence and dynamical origin of their source region would explain why they seem to always reach this threshold size of 5 μm, whatever the season or time of the day.

[90] Hence, the thickest parts of the cloud belt contain two different groups of clouds. First, large scale clouds formed by the regional wind circulation, characterized by particle sizes of 2–3.5 μm (the first group of retrievals in Figure 11), and found in the periphery of the cloud belt. Second, localized clouds formed over sloping regions, strongly controlled by local dynamics and composed of larger particles (r_{eff} = 5 μm, second group in Figure 11).

6. Conclusions

[91] The development of the aphelion cloud belt over the Tharsis plateau has been analyzed using the OMEGA near-infrared imaging spectrometer.

[92] The main results can be summarized as follows:

[93] 1. Global maps of the aphelion cloud belt in the Tharsis region are generated using the so-called cloud index. This cloud index is given by the ratio of the reflectance at 3.4 μm to that at 3.52 μm [*Langevin et al.*, 2007]. It reflects the cloud particle size and opacity. Four main types of clouds are identified: *morning hazes*, *topographically controlled hazes*, *cumulus clouds* and *thick hazes*. *Morning hazes* are homogeneous and found over regions of high albedo and low

thermal inertia, where the nighttime temperature is the coldest. They are probably remnants of nighttime clouds and dissipate by noon. *Topographically controlled hazes* are thin hazes found on sloping regions at various local times, before and after the formation of the optically dense cloud belt. They might have the same origin as the well developed cloud belt, but seem to be weakened by the high temperatures of early spring and late summer and resulting difficulty to reach saturation. *Cumulus clouds* are 5 to 10 km in size, and form during early afternoon from mid-spring to mid-summer. These are the times when the boundary layer is the thickest, and the saturation altitude the lowest. Their time of occurrence is consistent with the shallow convective origin proposed by *Michaels and Rafkin* [2004], even though this needs to be confirmed using spectral observations at higher spatial resolution. They are found especially south of Alba Patera and Valles Marineris and coexist with thick hazes at the periphery of the cloud belt. Consequently, they might explain the origin of the type 1 clouds identified by *Clancy et al.* [2003]. *Thick hazes* are found in the afternoon, and develop from mid-spring to mid-summer, especially west of the Tharsis Montes and north of Valles Marineris. They are the only clouds we are able to analyze in detail with OMEGA, given their large optical depth. They are especially well developed around $L_s = 100°$, as noticed by *Benson et al.* [2003], *Smith* [2004], and *Mateshvili et al.* [2007].

[94] 2. The effective radius of ice particles, cloud opacity at visible wavelengths and water ice content (WIC) are retrieved in the thickest parts of the cloud belt. The relative error on retrieved parameters is less than 30% for $r_{\mathrm{eff,ice}}$, and 20% for τ_{ice}. The same area has to be observed under cloud-free and cloudy conditions to deduce the cloud properties. The cloud-free spectrum is used to deduce the surface albedo, over which a synthetic cloud spectrum is fitted to the observed cloud spectrum. This is done by removing the contribution of atmospheric dust, using the dust opacity measurements made simultaneously by the MERs, and by accounting for thermal emissions, using the temperatures of the Mars Climate Database v4.3. Extrapolating measurements from the rovers introduces a large error on the atmospheric dust content, which results in uncertainty on surface albedo. This uncertainty is the main source of error in the retrieval. The other main uncertainties are knowledge of the surface temperature and instrumental errors. A systematic bias toward ice particle sizes which are at most 20–30% too small is possible, due to the change in ice optical indices as a function of cloud temperature. Ice particle sizes are consistent with previous analyses, range from 2.2 to 5.4 μm, and belong to type 2 clouds reported by *Clancy et al.* [2003]. The WIC can be considered as maximal, since we focus on the densest part of the cloud belt, and is equal to 1.3–5.2 pr.μm.

[95] 3. Cloud particle sizes can be separated in two groups, of 2–3.5 and 5 μm, respectively. The first group may represent "background" hazes found in the cloud belt, whereas the second group may correspond to regions of enhanced cloud formation. Particle sizes of the second group appear to be quite constant over L_s and local time, and always close to 5 μm. The second group is observed mostly west of Ascraeus and Pavonis Mons and west of Lunae Planum. These are regions of strong anabatic winds and these large particles could be created in environments that are strongly controlled by local dynamics and topography. A good example is provided by the Tharsis volcanoes, described by *Michaels et al.* [2006] as "water pumps" where large particles form locally before being carried westward by the regional circulation. This kind of formation processes, enhanced by the local wind dynamics, would explain why these particles are larger than the others. It would also account for their quite constant size over time, since they would rapidly grow to reach a threshold size and leave their formation environment.

[96] We emphasized in this study the complex evolution, in space and time, of the aphelion clouds, which display various morphologies and microphysical properties. This is a first attempt at monitoring cloud properties using near-infrared imaging spectrometry. The method described here could be applied to other regions, as long as ice is not present on the surface. The same approach could be used with CRISM/MRO, and coupled to its ability to acquire multiangle data. It would allow the extension of this analysis to thinner clouds, such as cumulus clouds.

[97] Limb observations with OMEGA could also be used to further characterize the vertical structure of these clouds. The stereo imaging provided by the HRSC/MEx instrument could also give access to the altitude of the different cloud types. The method consists of identifying the same pattern in two successive images. Then, the altitude of the cloud can be deduced with an uncertainty of $\sim$1 km [see *Scholten et al.*, 2010]. The high resolution profiles of MCS/MRO (Mars Climate Sounder) can also help us to understand the vertical structure of the clouds. The daytime evolution of the clouds will be explored in 2016, when the ExoMars Climate Sounder (EMCS) onboard the ExoMars Trace Gas Orbiter will provide the aerosol profiles and the water vapor content of the atmosphere at various local times.

[98] Clouds are essential indicators of Martian meteorological processes and provide an excellent way to evaluate climate models, as they result from a conjunction of factors including dynamics, tracer advection, temperature changes, and cloud microphysics. In the coming years, further multiscale observations and modeling of the aphelion clouds using Global Climate Models, mesoscale models and Large Eddy Simulations, will give fascinating insights into many key aspects of the Mars climate.

Appendix A: Retrieval Uncertainties

[99] A good way to clarify the possible biases of our retrieval method is to summarize it using the formalism of *Rodgers* [2000]. In this context, the result of the retrieval $\hat{\mathbf{x}}$ is written as follows:

$$\hat{\mathbf{x}} = \mathbf{R}\left(\mathbf{f}(\mathbf{x},\mathbf{b}) + \epsilon, \hat{\mathbf{b}}, \mathbf{x}_a, \mathbf{c}\right), \tag{A1}$$

where $\mathbf{R}$ is the retrieval algorithm, $\mathbf{f}$ the forward model (the DISORT radiative transfer code), $\mathbf{x}$ the free parameters ($r_{\mathrm{eff,ice}}$ and τ_{ice}), $\mathbf{b}$ the forward model parameters, ϵ the instrumental errors, $\mathbf{x}_a$ the a-priori information on the retrieved parameters and $\mathbf{c}$ the retrieval method parameters. The estimated quantities are distinguished from the true quantities by circumflexes. The present appendix describes each term of equation (A1) to provide an assessment of the resulting uncertainty in the retrieval $\hat{\mathbf{x}}$. A summary is given in section A4.

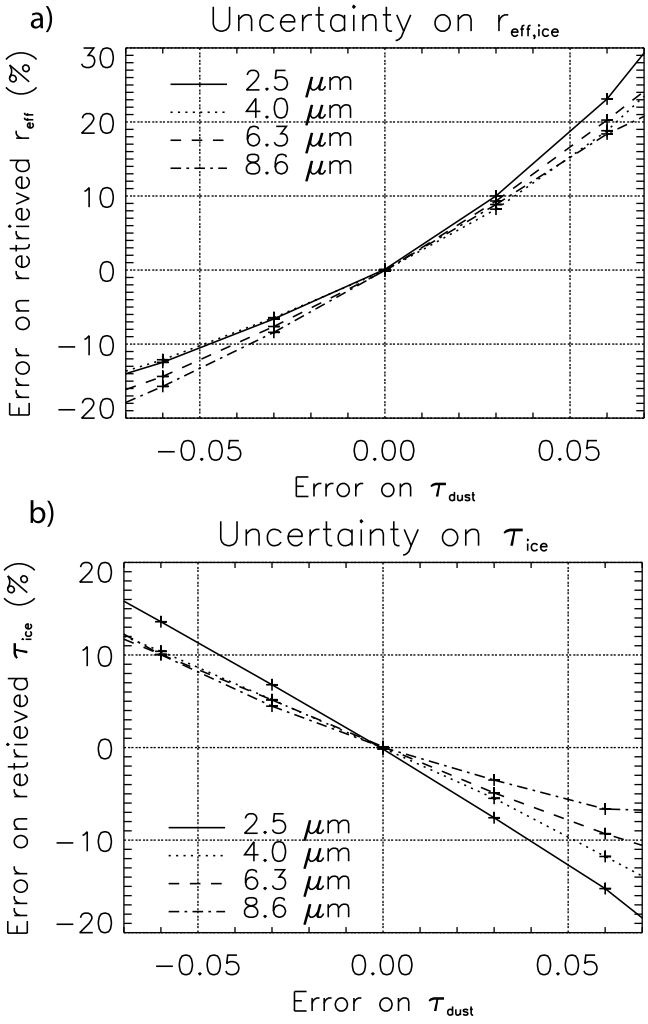

Figure A1. Relative error on the (a) retrieved ice particle size and (b) cloud opacity due to the uncertainty on dust opacity. The fitted cloud spectra are generated by the radiative transfer code for different ice particle sizes and optical depths. Four sizes are represented, and cloud optical depth is unity. The largest absolute error on $r_{\mathrm{eff,ice}}$ is ± 1.8 μm, and only applies for large particle sizes (around 8 μm).

A1. Instrumental Error (ϵ)

[100] To compute the OMEGA radiance, the raw data (in DN) is divided by the instrumental transfer function (ITF). From equation (1) of section 2, we can deduce the error in the reflectance that results from the instrumental error:

$$\sigma_{\Omega} = \Delta r_s = r_s\left(\frac{\Delta \mathrm{DN}}{\mathrm{DN}} + \frac{\Delta \mathrm{ITF}}{\mathrm{ITF}}\right), \tag{A2}$$

where the uncertainties in the incidence angle and solar radiance (see equation (1)) are neglected. Indeed, the incidence angle, as well as the emergence and phase angles, are known with a precision of 10^{-3} rad. As for the solar radiance, the data set of *Colina et al.* [1996] is used and its uncertainty is neglected, since our method is based on the comparison of two reflectances (surface albedo and cloud reflectance) computed using the same solar radiance. The only difference between the two reflectance spectra is the scaling factor used to deduce the solar radiance at Mars distance from the radiance at Earth's distance measured by *Colina et al.* [1996]. This distance is well constrained, and the resulting uncertainty is negligible. Therefore, the instrumental error only results from noise and error in the ITF, as described by equation (A2).

A1.1. Instrumental Noise

[101] The OMEGA signal noise is dominated by read noise, and the other sources of error are relatively minor [*Langevin et al.*, 2007]. An uncertainty of 2 DN is introduced [*Forget et al.*, 2007], whose effect on reflectance depends on the digital numbers received at the wavelength considered. For example, the effect of the constant read noise on the reflectance in the L channel is more important than for the C channel because of the weaker signal received at longer wavelengths. The less impacted wavelength is 1.5 μm, where the peak of the received signal occurs.

A1.2. Detector Nonlinearity

[102] In the 1.5 μm band region, another bias must be added and is caused by the nonlinearity of the detector when signal strength exceeds 1200 DN. This nonlinearity results in a relative error on the absorption band depth of water ice of 2 to 3% [*Jouglet et al.* 2007, para. 22]. Therefore, another uncertainty is added at 1.5 μm when DN > 1200 and is deduced from the relative error on the water ice absorption band depth ΔBD/BD as follows:

$$\sigma_{\Omega,1.5\mu\mathrm{m}} = \frac{\Delta I_{1.5\mu\mathrm{m}}}{\mu_0 I_{Sun}} = \frac{\Delta \mathrm{BD}}{\mathrm{BD}} \frac{\left(I_{1.18\mu\mathrm{m}} I_{1.73\mu\mathrm{m}}\right)^{1/2} - I_{1.5\mu\mathrm{m}}}{\mu_0 I_{Sun}},$$

where the absorption band depth BD is defined as:

$$\mathrm{BD} = 1 - \frac{I_{1.5\mu\mathrm{m}}}{\left(I_{1.18\mu\mathrm{m}} I_{1.73\mu\mathrm{m}}\right)^{1/2}}. \tag{A3}$$

[103] The radiance of the continuum used to compute the absorption band depth is given by the geometric mean of the two adjacent wavelengths among the seven used for our retrieval: $\left(I_{1.18\mu\mathrm{m}} I_{1.73\mu\mathrm{m}}\right)^{1/2}$. As the absorption band depth increases so does the effect of nonlinearity. The resulting uncertainty at 1.5 μm is often comparable to those introduced at other wavelengths by read noise only.

A1.3. Transfer Function Uncertainty

[104] Uncertainty in the ITF is negligible, except in the L channel where the photometric response is unstable for many observations. The correction method described by *Jouglet et al.* [2009] is used in the present work. It allows the correction of non-nominal observations up to orbit 7790. When a new ITF needs to be computed using this method, a relative error ΔITF/ITF = 1% is introduced, based on the analysis of *Jouglet et al.* [2009, Figure 9b].

A1.4. Total Instrumental Error

[105] The total instrumental error on the retrieved reflectance is shown in Figure 6 and especially noticed in the L channel. In the example shown in Figure 6, all the uncertainties mentioned above are introduced, and the mean

instrumental error is about 0.2%. The resulting error on the retrieved parameter is relatively small (±3% for both $r_{eff,ice}$ and τ_{ice}) compared to the error introduced by the forward model parameters, as we show next.

A2. Forward Model Parameters ($\hat{\mathbf{b}}$)

[106] As glimpsed in Figure 8, the radiative transfer code requires a set of inputs that have associated uncertainties. They are described below, in order of decreasing uncertainty.

A2.1. Surface Albedo (A_s) and Dust Correction

[107] The largest uncertainty of our study lies on the retrieved surface albedo A_s (see section 4.1.6). Indeed, it depends on the assumed dust opacity and radiative properties used to remove the contribution of dust scattering from the cloud-free observation. *Vincendon et al.* [2009] studied atmospheric dust using the OMEGA spectrometer, and developed a method to retrieve dust opacity using different observations of the same area. It is impossible to use the same method in our case, since the probability of finding multiple cloud-free spectra plus a cloud spectrum in the same area is too small. Nevertheless, *Vincendon et al.* [2009] compared the Mars Exploration Rover dust opacity with a series of OMEGA measurements for different dark regions and scaled to an equivalent surface pressure. From these results it seems that using the rover dust opacity to deduce the opacity in any area of the low to midlatitudes (what we do) is accurate to within ±0.1. Scaled to the mean altitude of the Tharsis plateau (which is the focus of our study), this is equivalent to a 1-σ error on dust opacity of ±0.07.

[108] To quantify the uncertainty resulting from this error on dust opacity and, a fortiori, surface albedo, we generate a set of synthetic cloud spectra for which $r_{eff,ice}$ and τ_{ice} are known, and try to recover these two parameters using our retrieval method. To generate these synthetic cloud spectra, the surface albedo retrieved for orbit 3741_4, which corresponds to a dust opacity of 0.42, is used as a lower boundary condition. When there is no error on the dust opacity assumed for retrieval (i.e. when $\tau_{dust} = 0.42$), the retrieved $r_{eff,ice}$ and τ_{ice} are equal to those used to generate the synthetic cloud spectra, and the retrieval error is zero. However, when a perturbation in dust opacity is introduced in the retrieval algorithm (i.e. $\tau_{dust} = 0.42 \pm 0.07$), the surface albedo is not determined accurately. Therefore, the retrieved $r_{eff,ice}$ and τ_{ice} depart from the ones used for cloud spectra calculation, and the retrieval error can be assessed.

[109] The results of this experiment are summarized in Figure A1, which represents the relative error on $r_{eff,ice}$ and τ_{ice} as a function of dust opacity perturbation. Four different ice particle sizes are employed and the optical depth at 0.67 μm is unity. When dust opacity is overestimated, so is the retrieved ice particle size. Indeed, Tharsis terrains are relatively bright and adding dust tends to darken the surface. When dust opacity is overestimated, the retrieved surface albedo is higher than what it should be. Consequently, in the retrieval process the level of the continuum is too high and the minimization algorithm increases the absorption band depths to fit the cloud spectrum, resulting in an overestimated particle size. Similar reasoning applies when dust opacity is underestimated, explaining the general trend seen in Figure A1a.

[110] On the contrary, overestimating dust opacity results in an underestimated cloud opacity, as shown by Figure A1b. This is a direct consequence of the aforementioned effect: overestimating dust opacity results in larger ice particles and larger absorption coefficient. The retrieved cloud opacity is thus reduced accordingly.

[111] Using the uncertainty on dust opacity of ±0.07 introduced above, the relative error on the ice particle size $r_{eff,ice}$ is less than 30%, and less than 20% for the cloud opacity τ_{ice}.

[112] It is essential to note that these uncertainties depend on the cloud particle size and opacity, and are given here for a cloud opacity of 1. Uncertainty increases with decreasing cloud opacity. This is explained by the fact that the surface appears through the clouds as cloud opacity decreases, thereby increasing the impact of the error made on surface albedo. For example, an absolute error of around ±3 μm is made for a particle size of 6 μm if cloud opacity is reduced to 0.5. Therefore, our method is valid for cloud opacity near unity.

[113] It is finally worth mention that we assume uniform mixing of the dust. We tested the sensitivity of our method to different Conrath distributions [*Conrath*, 1975] and dust layer thicknesses, and did not observe any significant changes in the retrievals.

A2.2. Cloud Scattering Properties and Altitude

[114] The single scattering parameters for different sizes of ice particles are deduced from the water ice optical indices of *Warren* [1984] measured at 270 K (see section 4.1.7). However, ice indices vary with temperature, which is nearly equal to or lower than 180 K in Martian clouds. The optical indices of *Warren* [1984] are often used for Martian studies but one must be careful when working in the near-infrared range, where the dependence on temperature is not negligible [*Warren*, 1984; *Grundy and Schmitt*, 1998]. The effect of temperature on the imaginary index of water ice is represented in Figure A2. The two extreme temperatures of 145 K [*Grundy and Schmitt*, 1998; *Schmitt et al.*, 1998] and 270 K [*Warren*, 1984] are represented in black and gray, respectively. As temperature increases, so does the imaginary index outside the absorption bands. Consequently, absorption by water ice crystals increases with temperature.

[115] When the optical indices of *Warren* [1984] are replaced by the 145 K optical indices of *Grundy and Schmitt* [1998], our method is less accurate, and the χ^2 value is increased by a factor of ~1.6. This probably results from the temperature of 145 K, which is too low. Using the optical indices of ice at 180 K would probably improve the results, but at this temperature, the optical indices can not be easily measured at wavelengths longer than 2.7 μm [*Grundy and Schmitt*, 1998], preventing us from using the L channel.

[116] We compared two sets of retrievals made using the two different optical indices, and found that the retrieved ice particle size is the most affected. We estimate that the use of the 270 K ice optical indices could introduce a systematic bias toward ice particle sizes which are 20–30% too small. This bias is maximal and probably overestimated, because the temperature of 145 K used to make our assessment is

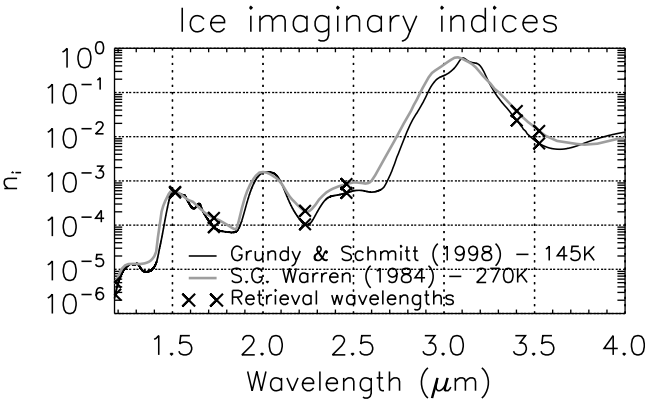

Figure A2. Imaginary indices n_i of hexagonal water ice measured by *Grundy and Schmitt* [1998] and *Schmitt et al.* [1998] (black curve) and *Warren* [1984] (gray curve). The sample temperatures are 145 K and 270 K, respectively. Times symbols indicate the n_i values for the wavelengths used in the retrieval. Ice temperature changes the sharpness of the absorption bands and has a non-negligible effect on the retrieved ice particle sizes.

colder than the mean expected temperature of Martian clouds.

[117] Other possible sources of uncertainty, such as the cloud altitude or effective variance of the ice particle distribution, were considered but did not have a significant impact on the retrievals.

A2.3. Thermal Contribution

[118] The thermal contribution in the L channel is accounted for by using the MCD v4.3 [*Forget et al.*, 1999; *Millour et al.*, 2008] surface and atmospheric temperatures. Thermal emission mainly depends on surface temperature, which is controlled by surface thermal inertia and albedo, rather than by slope or altitude [see, e.g., *Putzig and Mellon*, 2007, Figure 1]. Local variations in these two quantities may result in surface temperature differences not captured by the LMD/GCM (the Global Climate Model used to build the MCD). Indeed, the LMD/GCM uses $\sim$300 $\times$ 200 km grid boxes at equatorial latitudes, and thereby misses the subgrid scale temperature variations seen at OMEGA resolution.

[119] To assess the resulting bias, *Forget et al.* [2007] compared the MCD surface temperatures to the OMEGA measurements of *Jouglet et al.* [2009, section 4.3], and found that local differences due to surface property inhomogeneities are lower than 10 K. We therefore tested the sensitivity of our retrieval to a 1-σ error in surface temperature of 5 K. The resulting uncertainty on ice particle size is estimated at $\pm$0.2 μm, and at $\pm$0.05 for cloud opacity.

A2.4. Dust Radiative Properties

[120] As explained in section 4.1.4, the dust single scattering parameters are computed from the refractive index of *Wolff et al.* [2009] by the T-Matrix code of *Mishchenko et al.* [1996]. The dominant error source is not the uncertainty in the refractive index in our case, but rather the assumption on the size distribution of the dust particles made for computing the single scattering parameters. The retrieval results for different shapes of the distribution (Gamma or lognormal) or shapes of the dust particles (spheres or cylinders) differ by less than 2%. The same can be said for a $\pm$0.1 change in the effective variance of the distribution.

[121] The effective radius of the size distribution has a much larger impact on the retrieval results, which differ by $\sim$10% for a $\pm$0.5 μm change in the dust particle size around the default value of 1.5 μm. This difference can be mainly attributed to an increase in the absorption coefficient with increasing size of the dust particles. The asymmetry factor g is, on the contrary, nearly unchanged, at least in the OMEGA wavelength range. Therefore, overestimating dust particle size is similar to overestimating dust opacity. We thus consider that the error due to the uncertainty on dust particle size is already accounted for by the uncertainty on dust opacity, which was introduced earlier.

A2.5. Observing Geometry (i.e., φ)

[122] The OMEGA observing geometry is known with an accuracy of 10^{-3} rad, and the resulting uncertainty on our retrieval is negligible and always lower than $\pm$1%.

A2.6. Surface Hydration

[123] Hydration of surface minerals has many absorption bands, the strongest of which is the 3 μm absorption band. This band is extensively studied on Mars, as an indicator of the surface water content [*Jouglet et al.*, 2007; *Milliken et al.*, 2007; *Pommerol et al.*, 2009; *Beck et al.*, 2010]. Our retrieval uses the 3.1 μm band of water ice, which could be affected by the 3 μm hydration band. However, *Jouglet et al.* [2007] analyzed the seasonal variations in the 3 μm hydration band, and found that, except in the 40°N–60°N latitude band, the 3 μm signature due to surface hydration remains unchanged from one observation to the other. Our region of study is outside this latitude band. We can therefore assume that the surface hydration state is the same for the two spectra used in our retrieval and that surface hydration has no impact on cloud property measurements.

A3. Retrieval Method Parameters

A3.1. A Priori Information (x_a)

[124] The result of the retrieval does not depend on the a-priori information, as long as the initial size of the ice particles is larger than a micrometer. Otherwise, the minimization algorithm stops in a secondary minimum, as explained in the last paragraph of section 4.1.7.

A3.2. Minimization Parameters (c)

[125] The minimization method stops when the relative difference between two consecutive solutions is less than 0.1%. The step size used to compute numerical derivatives is 0.5 μm for $r_{\mathrm{eff,ice}}$ and 0.1 for τ_{ice}. Other values within the same order of magnitude do not change the results by more than 1%. Therefore, there is no significant uncertainty introduced by the minimization.

A4. Overall Uncertainty

[126] In summary, the main sources of uncertainty are the instrumental error and the errors on dust opacity (and therefore on the retrieved surface albedo) and temperature. The total 1-σ error is obtained by quadratically adding these

three errors, and is summarized in Table 3 for different ice particle sizes and a cloud opacity of unity. The relative error is about 25% for $r_{\mathrm{eff,ice}}$ and 15% for τ_{ice}. There is also a possible systematic bias toward ice crystals which are 20–30% too small, due to the uncertainty on water ice optical indices.

[127] **Acknowledgments.** Very helpful and constructive advice regarding the text was provided by Todd Clancy and an anonymous reviewer, and by Pascal Rannou and Peter Read. We express our gratitude to A. Määttänen, F. Poulet and T. Appéré for very useful discussions. We thank Nicolas Mangold and Thierry Fouchet who have provided continuous and thoughtful support for this work and the associated thesis. We also acknowledge continuous support from the teams of the LMD, IAS and IPSL supercomputing facilities (R. Franchisseur, V. Fabart, P. Weill, G. Poulleau). We are also grateful to the Mars Express and OMEGA teams who made this project possible. Grant support for this work was provided by the UPMC university through doctoral fellowship and by ESA and CNES.

References

Beck, P., A. Pommerol, B. Schmitt, and O. Brissaud (2010), Kinetics of water adsorption on minerals and the breathing of the Martian regolith, *J. Geophys. Res.*, *115*, E10011, doi:10.1029/2009JE003539.

Benson, J. L., B. P. Bonev, P. B. James, K. J. Shan, B. A. Cantor, and M. A. Caplinger (2003), The seasonal behavior of water ice clouds in the Tharsis and Valles Marineris regions of Mars: Mars Orbiter Camera Observations, *Icarus*, *165*, 34–52.

Benson, J. L., P. B. James, B. A. Cantor, and R. Remigio (2006), Interannual variability of water ice clouds over major Martian volcanoes observed by MOC, *Icarus*, *184*, 365–371.

Bibring, J., et al. (2004), OMEGA: Observatoire pour la Minéralogie, l'Eau, les Glaces et l'Activité, *Eur. Space Agency Spec. Publ.*, *ESA SP-1240*, 37–49.

Briggs, G. A., and C. B. Leovy (1974), Mariner Observations of the Mars North Polar Hood., *Bull. Am. Meteorol. Soc.*, *55*, 278–2784.

Christensen, P. R. (1998), Variations in Martian surface composition and cloud occurrence determined from thermal infrared spectroscopy: Analysis of Viking and Mariner 9 data, *J. Geophys. Res.*, *103*, 1733–1746.

Christensen, P. R., et al. (2001), Mars Global Surveyor Thermal Emission Spectrometer experiment: Investigation description and surface science results, *J. Geophys. Res.*, *106*, 23,823–23,872.

Clancy, R. T., A. W. Grossman, M. J. Wolff, P. B. James, D. J. Rudy, Y. N. Billawala, B. J. Sandor, S. W. Lee, and D. O. Muhleman (1996), Water vapor saturation at low altitudes around Mars aphelion: A key to Mars climate?, *Icarus*, *122*, 36–62.

Clancy, R. T., B. J. Sandor, M. J. Wolff, P. R. Christensen, M. D. Smith, J. C. Pearl, B. J. Conrath, and R. J. Wilson (2000), An intercomparison of ground-based millimeter, MGS TES, and Viking atmospheric temperature measurements: Seasonal and interannual variability of temperatures and dust loading in the global Mars atmosphere, *J. Geophys. Res.*, *105*, 9553–9572.

Clancy, R. T., M. J. Wolff, and P. R. Christensen (2003), Mars aerosol studies with the MGS TES emission phase function observations: Optical depths, particle sizes, and ice cloud types versus latitude and solar longitude, *J. Geophys. Res.*, *108*(E9), 5098, doi:10.1029/2003JE002058.

Colaprete, A., and O. B. Toon (2000), The radiative effects of Martian water ice clouds on the local atmospheric temperature profile, *Icarus*, *145*, 524–532.

Colaprete, A., O. B. Toon, and J. A. Magalhães (1999), Cloud formation under Mars Pathfinder conditions, *J. Geophys. Res.*, *104*, 9043–9054.

Colina, L., R. C. Bohlin, and F. Castelli (1996), The 0.12–2.5 micron Absolute Flux Distribution of the Sun for Comparison With Solar Analog Stars, *Astron. J.*, *112*, 307–315.

Conrath, B. J. (1975), Thermal structure of the Martian atmosphere during the dissipation of the dust storm of 1971, *Icarus*, *24*, 36–46.

Curran, R. J., B. J. Conrath, R. A. Hanel, V. G. Kunde, and J. C. Pearl (1973), Mars: Mariner 9 spectroscopic evidence for H_2O ice clouds, *Science*, *182*, 381–383.

Encrenaz, T., et al. (2005), A mapping of Martian water sublimation during early northern summer using OMEGA/Mars Express, *Astron. Astrophys.*, *441*, L9–L12.

Fedorova, A., O. Korablev, J.-L. Bertaux, A. Rodin, A. Kiselev, and S. Perrier (2006), Mars water vapor abundance from SPICAM IR spectrometer: Seasonal and geographic distributions, *J. Geophys. Res.*, *111*, E09S08, doi:10.1029/2006JE002695.

Fenton, L. K., P. E. Geissler, and R. M. Haberle (2007), Global warming and climate forcing by recent albedo changes on Mars, *Nature*, *446*, 646–649.

Forget, F., F. Hourdin, R. Fournier, C. Hourdin, O. Talagrand, M. Collins, S. R. Lewis, P. L. Read, and J.-P. Huot (1999), Improved general circulation models of the Martian atmosphere from the surface to above 80 km, *J. Geophys. Res.*, *104*, 24,155–24,176.

Forget, F., et al. (2007), Remote sensing of surface pressure on Mars with the Mars Express/OMEGA spectrometer: 1. Retrieval method, *J. Geophys. Res.*, *112*, E08S15, doi:10.1029/2006JE002871.

Glenar, D. A., R. E. Samuelson, J. C. Pearl, G. L. Bjoraker, and D. Blaney (2003), Spectral imaging of Martian water ice clouds and their diurnal behavior during the 1999 aphelion season (Ls = 130°), *Icarus*, *161*, 297–318.

Grundy, W. M., and B. Schmitt (1998), The temperature-dependent near-infrared absorption spectrum of hexagonal H2O ice, *J. Geophys. Res.*, *103*, 25,809–25,822.

Haberle, R. M., et al. (1999), General circulation model simulations of the Mars Pathfinder atmospheric structure investigation/meteorology data, *J. Geophys. Res.*, *104*, 8957–8974.

Hechler, M., and A. Yanez (2003), Mars express orbit design, *Acta Astronaut.*, *53*, 497–507.

Herschel, W. (1784), On the remarkable Appearances at the Polar Regions of the Planet Mars, the Inclination of its Axis, the Position of its Poles, and its spheroidical figure; with a few Hints relating to its real Diameter and Atmosphere, *Philos. Trans. R. Soc. London*, *74*, 233–273.

Hinson, D. P., and R. J. Wilson (2004), Temperature inversions, thermal tides, and water ice clouds in the Martian tropics, *J. Geophys. Res.*, *109*, E01002, doi:10.1029/2003JE002129.

Hunt, G. E., A. O. Pickersgill, P. B. James, and G. Johnson (1980), Some diurnal properties of clouds over the Martian volcanoes, *Nature*, *286*, 362–364.

Iraci, L. T., B. D. Phebus, B. M. Stone, and A. Colaprete (2010), Water ice cloud formation on Mars is more difficult than presumed: Laboratory studies of ice nucleation on surrogate materials, *Icarus*, *210*, 985–991.

Jouglet, D., F. Poulet, R. E. Milliken, J. F. Mustard, J.-P. Bibring, Y. Langevin, B. Gondet, and C. Gomez (2007), Hydration state of the Martian surface as seen by Mars Express OMEGA: 1. Analysis of the 3 micron hydration feature, *J. Geophys. Res.*, *112*, E08S06, doi:10.1029/2006JE002846.

Jouglet, D., F. Poulet, Y. Langevin, J.-P. Bibring, B. Gondet, M. Vincendon, and M. Berthe (2009), OMEGA long wavelength channel: Data reduction during non-nominal stages, *Planet. Space Sci.*, *57*, 1032–1042.

Kahn, R. (1984), The spatial and seasonal distribution of Martian clouds and some meteorological implications, *J. Geophys. Res.*, *89*, 6671–6688.

Langevin, Y., J. Bibring, F. Montmessin, F. Forget, M. Vincendon, S. Douté, F. Poulet, and B. Gondet (2007), Observations of the south seasonal cap of Mars during recession in 2004–2006 by the OMEGA visible/near-infrared imaging spectrometer on board Mars Express, *J. Geophys. Res.*, *112*, E08S12, doi:10.1029/2006JE002841.

Lefèvre, F., J. Bertaux, R. Clancy, T. Encrenaz, K. Fast, F. Forget, S. Lebonnois, F. Montmessin, and S. Perrier (2008), Heterogeneous chemistry in the atmosphere of Mars, *Nature*, *454*(7207), 971–975.

Lemmon, M. T., et al. (2004), Atmospheric Imaging Results from the Mars Exploration Rovers: Spirit and Opportunity, *Science*, *306*, 1753–1756.

Leovy, C. B., G. A. Briggs, and B. A. Smith (1973), Mars atmosphere during the Mariner 9 extended mission: Television results, *J. Geophys. Res.*, *78*, 4252–4266.

Määttänen, A., H. Vehkamäki, A. Lauri, S. Merikallio, J. Kauhanen, H. Savijärvi, and M. Kulmala (2005), Nucleation studies in the Martian atmosphere, *J. Geophys. Res.*, *110*, E02002, doi:10.1029/2004JE002308.

Maltagliati, L., D. V. Titov, T. Encrenaz, R. Melchiorri, F. Forget, M. Garcia-Comas, H. U. Keller, Y. Langevin, and J. Bibring (2008), Observations of atmospheric water vapor above the Tharsis volcanoes on Mars with the OMEGA/MEx imaging spectrometer, *Icarus*, *194*, 53–64.

Markwardt, C. B. (2009), Non-linear least-squares fitting in IDL with MPFIT, in *Astron. Soc. Pac. Conf. Ser.*, vol. 411, edited by D. Bohlender, P. Dowler, and D. Durand, pp. 251–254, Astron. Soc. of the Pac., San Francisco, Calif.

Mateshvili, N., D. Fussen, F. Vanhellemont, C. Bingen, J. Dodion, F. Montmessin, S. Perrier, E. Dimarellis, and J. Bertaux (2007), Martian ice cloud distribution obtained from SPICAM nadir UV measurements, *J. Geophys. Res.*, *112*, E07004, doi:10.1029/2006JE002827.

Michaels, T. I. (2008), Complexities of modeled water ice clouds near Olympus Mons, Mars, presented at the Mars Water Cycle Workshop, Eur. Space Agency, Paris, 21–23 April.

Michaels, T. I., and S. C. R. Rafkin (2004), Large-eddy simulation of atmospheric convection on Mars, *Q. J. R. Meteorol. Soc.*, *130*, 1251–1274.

Michaels, T. I., A. Colaprete, and S. C. R. Rafkin (2006), Significant vertical water transport by mountain-induced circulations on Mars, *Geophys. Res. Lett.*, *33*, L16201, doi:10.1029/2006GL026562.

Michelangeli, D. V., O. B. Toon, R. M. Haberle, and J. B. Pollack (1993), Numerical simulations of the formation and evolution of water ice clouds in the Martian atmosphere, *Icarus*, *102*, 261–285.

Milliken, R. E., J. F. Mustard, F. Poulet, D. Jouglet, J. Bibring, B. Gondet, and Y. Langevin (2007), Hydration state of the Martian surface as seen by Mars Express OMEGA: 2. H_2O content of the surface, *J. Geophys. Res.*, *112*, E08S07, doi:10.1029/2006JE002853.

Millour, E., et al. (2008), The latest (version 4.3) Mars climate database, *LPI Contrib.*, *1447*, Abstract 9029.

Mishchenko, M. I., L. D. Travis, and D. W. Mackowski (1996), T-matrix computations of light scattering by nonspherical particles: A review., *J. Quant. Spectrosc. Radiat. Transfer*, *55*, 535–575.

Montmessin, F., F. Forget, P. Rannou, M. Cabane, and R. M. Haberle (2004), Origin and role of water ice clouds in the Martian water cycle as inferred from a general circulation model, *J. Geophys. Res.*, *109*, E10004, doi:10.1029/2004JE002284.

Moré, J., D. Sorenson, B. Garbow, and K. Hillstrom (1984), The MINPACK project, in *Sources and Development of Mathematical Software*, edited by W. J. Cowell, pp. 88–111, Prentice-Hall, Upper Saddle River, N. J.

Pearl, J. C., M. D. Smith, B. J. Conrath, J. L. Bandfield, and P. R. Christensen (2001), Observations of Martian ice clouds by the Mars Global Surveyor Thermal Emission Spectrometer: The first Martian year, *J. Geophys. Res.*, *106*, 12,325–12,338.

Petrova, E., H. U. Keller, W. J. Markiewicz, N. Thomas, and M. W. Wuttke (1996), Ice hazes and clouds in the Martian atmosphere as derived from the Phobos/KRFM data, *Planet. Space Sci.*, *44*, 1163–1176.

Pommerol, A., B. Schmitt, P. Beck, and O. Brissaud (2009), Water sorption on Martian regolith analogs: Thermodynamics and near-infrared reflectance spectroscopy, *Icarus*, *204*, 114–136.

Putzig, N. E., and M. T. Mellon (2007), Apparent thermal inertia and the surface heterogeneity of Mars, *Icarus*, *191*, 68–94.

Putzig, N. E., M. T. Mellon, K. A. Kretke, and R. E. Arvidson (2005), Global thermal inertia and surface properties of Mars from the MGS mapping mission, *Icarus*, *173*, 325–341.

Richardson, M. I., R. J. Wilson, and A. V. Rodin (2002), Water ice clouds in the Martian atmosphere: General circulation model experiments with a simple cloud scheme, *J. Geophys. Res.*, *107*(E9), 5064, doi:10.1029/2001JE001804.

Rodgers, C. (2000), *Inverse Methods for Atmospheric Sounding: Theory and Practice*, World Sci., Singapore.

Schmitt, B., E. Quirico, F. Trotta, and W. M. Grundy (1998), Optical Properties of Ices from UV to Infrared, in *Solar System Ices*, *Astrophys. Space Sci. Libr.*, vol. 227, edited by B. Schmitt, C. de Bergh, and M. Festou, p. 199, Kluwer Acad., Dordrecht, Netherlands.

Scholten, F., H. Hoffmann, A. Määttänen, F. Montmessin, B. Gondet, and E. Hauber (2010), Concatenation of HRSC colour and OMEGA data for the determination and 3D-parameterization of high-altitude CO_2 clouds in the Martian atmosphere, *Planetary Space Sci.*, *58*, 1207–1214.

Smith, M. D. (2004), Interannual variability in TES atmospheric observations of Mars during 1999–2003, *Icarus*, *167*, 148–165.

Smith, M. D. (2009), THEMIS observations of Mars aerosol optical depth from 2002–2008, *Icarus*, *202*, 444–452.

Spiga, A., and F. Forget (2009), A new model to simulate the Martian mesoscale and microscale atmospheric circulation: Validation and first results, *J. Geophys. Res.*, *114*, E02009, doi:10.1029/2008JE003242.

Spiga, A., et al. (2007), Remote sensing of surface pressure on Mars with the Mars Express/OMEGA spectrometer: 2. Meteorological maps, *J. Geophys. Res.*, *112*, E08S16, doi:10.1029/2006JE002870.

Spiga, A., F. Forget, S. R. Lewis, and D. P. Hinson (2010), Structure and dynamics of the convective boundary layer on Mars as inferred from large-eddy simulations and remote-sensing measurements, *Q. J. R. Meteorol. Soc.*, *136*(647), 414–428.

Stamnes, K., S. Tsay, K. Jayaweera, and W. Wiscombe (1988), Numerically stable algorithm for discrete-ordinate-method radiative transfer in multiple scattering and emitting layered media, *Appl. Opt.*, *27*, 2502–2509.

Tamppari, L. K., R. W. Zurek, and D. A. Paige (2003), Viking-era diurnal water-ice clouds, *J. Geophys. Res.*, *108*(E7), 5073, doi:10.1029/2002JE001911.

Vincendon, M., Y. Langevin, F. Poulet, A. Pommerol, M. Wolff, J.-P. Bibring, B. Gondet, and D. Jouglet (2009), Yearly and seasonal variations of low albedo surfaces on Mars in the OMEGA/MEx dataset: Constraints on aerosols properties and dust deposits, *Icarus*, *200*, 395–405.

Wang, H., and A. P. Ingersoll (2002), Martian clouds observed by Mars Global Surveyor Mars Orbiter Camera, *J. Geophys. Res.*, *107*(E10), 5078, doi:10.1029/2001JE001815.

Warren, S. G. (1984), Optical constants of ice from the ultraviolet to the microwave, *Appl. Opt.*, *23*(8), 1206–1225.

Wilson, R. J., S. R. Lewis, L. Montabone, and M. D. Smith (2008), Influence of water ice clouds on Martian tropical atmospheric temperatures, *Geophys. Res. Lett.*, *35*, L07202, doi:10.1029/2007GL032405.

Wolff, M., and R. Clancy (2003), Constraints on the size of Martian aerosols from Thermal Emission Spectrometer observations, *J. Geophys. Res.*, *108*(E9), 5097, doi:10.1029/2003JE002057.

Wolff, M. J., R. T. Clancy, K. M. Pitman, J. F. Bell, and P. B. James (2001), Constraints on Martian aerosol particles using MGS/TES and HST data: Shapes, *Eos Trans. AGU*, *82*(47), Fall Meet. Suppl., Abstract P32E-05.

Wolff, M. J., et al. (2006), Constraints on dust aerosols from the Mars Exploration Rovers using MGS overflights and Mini-TES, *J. Geophys. Res.*, *111*, E12S17, doi:10.1029/2006JE002786.

Wolff, M. J., M. D. Smith, R. T. Clancy, R. Arvidson, M. Kahre, F. Seelos, S. Murchie, and H. Savijärvi (2009), Wavelength dependence of dust aerosol single scattering albedo as observed by the Compact Reconnaissance Imaging Spectrometer, *J. Geophys. Res.*, *114*, E00D04, doi:10.1029/2009JE003350.

Zasova, L., D. Grassi, V. Formisano, and A. Maturilli (2001), The Martian atmosphere in the region of the great volcanoes: Mariner 9 IRIS data revisited, *Planet. Space Sci.*, *49*, 977–992.

Zuber, M. T., D. E. Smith, S. C. Solomon, D. O. Muhleman, J. W. Head, J. B. Garvin, J. B. Abshire, and J. L. Bufton (1992), The Mars Observer laser altimeter investigation, *J. Geophys. Res.*, *97*, 7781–7797.

J.-P. Bibring, B. Gondet, D. Jouglet, Y. Langevin, and M. Vincendon, Institut d'Astrophysique Spatiale, Centre universitaire d'Orsay, Bat 120-121, Orsay F-91405, France.

F. Forget and A. Spiga, Laboratoire de Météorologie Dynamique, CNRS/UPMC/IPSL, 4 pl. Jussieu, Paris CEDEX 05, F-75005 France.

J.-B. Madeleine, Department of Geological Sciences, Brown University, 324 Brook St., Box 1846, Providence, RI 02912, USA. (jean-baptiste_madeleine@brown.edu).

F. Montmessin, LATMOS, CNRS/UVSQ/IPSL, Quartier des Garennes, 11 blvd. d'Alembert, F-78280 Guyancourt, France.

B. Schmitt, Laboratoire de Planétologie de Grenoble, UJF/CNRS, 122 rue de la Piscine, B.P. 53, Grenoble CEDEX 09, F-38041, France.

M. J. Wolff, Space Science Institute, 4750 Walnut St., #205, Boulder, CO 80301, USA.